AQUACULTURE NET

DRAG FORCE AND ADDED MASS SCALING

CHESLAV BALASH

AQUACULTURE NET

DRAG FORCE AND ADDED MASS SCALING

by Cheslav Balash

A Thesis

Submitted in Partial Fulfilment of the Requirements

For the Degree of

Master of Engineering

The School of Graduate Studies

Memorial University of Newfoundland

November 2007

Supervisory Committee:

Bruce Colbourne, Research Officer, National Research Council

Neil Bose, Professor of Naval Architecture and Ocean Engineering,
Memorial University of Newfoundland

Wayne Raman-Nair, Research Officer, National Research Council

Abstract

Five plane net samples of different geometry are selected and the hydrodynamic loads on them in quasi-static (steady current) and oscillating flow (harmonic waves) are measured in a towing tank and a wave basin. The data from the experiments is compared with existing empirical formulae and a numerical model. It is revealed that drag coefficients for nets and cylinders as a function of the Reynolds number have identical trends with steady offsets from each other. It is concluded that the drag coefficient for nets is equivalent to the drag coefficient for cylinders (and spheres for knotted nets) modified by a function of net porosity. A two-factorial experimental design was applied to screen individual and interaction effects of net solidity and steady current velocity. This analysis shows that solidity and velocity have a synergetic effect on drag. The drag component and added mass are extracted from the total wave force by applying a vector approach. It is shown that drag and added mass coefficients could not be expressed by conventional non-dimensional parameters. Based on data analysis, unsteady drag coefficient is suggested as a function of wave particle velocity and net porosity. It is recommended to estimate added mass through an effective thickness, the width of water affected by the net, which is a function of wave frequency and net solidity.

Acknowledgements

In addition to my Supervisory Committee, I acknowledge my appreciation to the staff of the Institute for Ocean Technology for their assistance in designing and conducting the experiments.

I would also like to thank Mike Sullivan from the Institute for Ocean Technology and Yuri Muzychka from Memorial University of Newfoundland for their support and interest in the project.

Table of Contents

List of Tables

List of Figures

Abbreviation and symbols

A	wave amplitude
A_p	projected area
C_D	drag coefficient
C_M	inertia coefficient
d	dimension of a body across the flow, twine diameter
D	knot diameter
F_A	added mass
F_D	drag force
F_T	total wave force
h	water depth
IA	image analysis
k	wave number
KC	Keulegan-Carpenter number
l	mesh size
MM	manual measurements
n	function of the net solidity
Re	Reynolds number
S	frontal area of a body
S_d	net solidity
T	wave period
U	water velocity, particle velocity in wave
Ŭ	particle acceleration
α	angle between the current direction and the net plane
δ	effective thickness
λ	wave length
ν	kinematic viscosity
ρ	water density
φ_a	acceleration phase
φ_u	velocity phase
ω	wave frequency

List of Appendices

I. Introduction and overview

Aquaculture has traditionally operated in near-shore locations on a small business scale. However, due to reductions in the world's fish stocks and continuously increasing food demand on a global scale, aquaculture is increasing in industrial scale. Particularly, according to the Canadian Aquaculture Industry Alliance, aquaculture is the fastest growing food industry in Canada and its value is expected to grow more than five times over the next ten years. Presently, the industry is considering the use of offshore ocean regions as an alternative to traditional near-shore locations. This innovation is motivated by the limitations of suitable coastal areas and environmental and aesthetic concerns. A move to open-ocean locations is expected to provide higher levels of environmental loading and thus it is essential to assess the behavior of open-ocean fish containment structures before they are exposed to these more severe environmental forces. Since, coastal fish farms have been located on sites protected from extreme currents and waves, comprehensive studies on large hydrodynamic forces applied on aquaculture structures in more extreme conditions have not previously been necessary.

Typically a fish farm presents a floating platform, which is moored to the seabed, with net cages attached to it (Fig 1.1). Previous experimental and numerical studies conducted in this area considered force estimation on entire net cages, mooring cables and plane net samples. Berteaux [5] and other researchers,

at different times, have extensively discussed normal and tangential forces on mooring lines and cables. Nets present a more complex type of flexible structure with multiple degrees of freedom that undergo large deformation under external and internal forces. A net changes its shape under hydrodynamic load, but as the shape changes, the loads are also changing. In other words, the net shape and forces have a complex non-linear effect on each other. These properties complicate the investigation of flow through and around the twine bars of a mesh structure and hydrodynamic loads applied on them. Due to this complex nature of the fluid forces on netting and since open-ocean aquaculture is a relatively recent innovation, loads on nets, especially in oscillating flow, are not yet comprehensively understood.

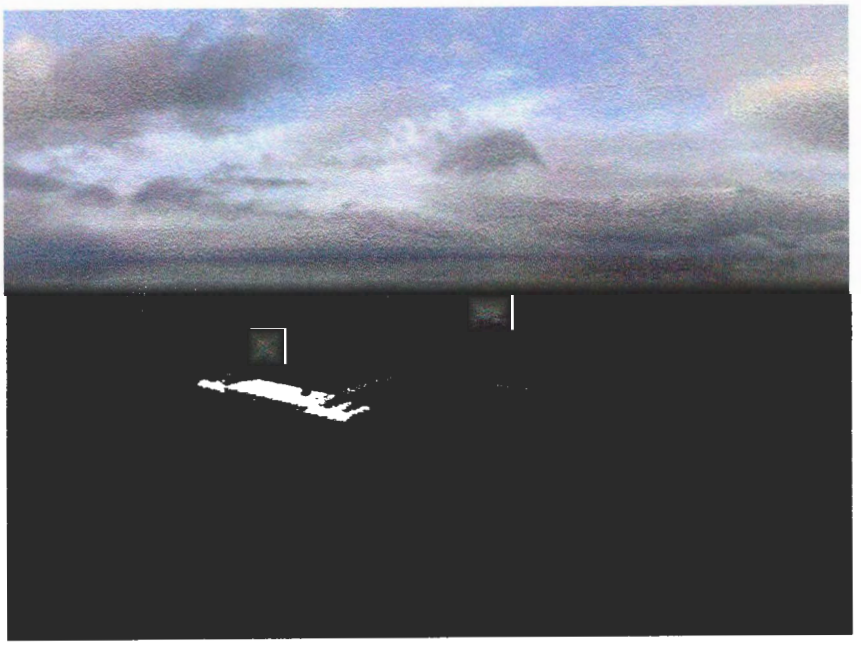

Fig. 1.1 Floating fish platform

There has been a volume of research conducted on cage modeling [4], [8], [11], [12], [13], but although these studies provide a better understanding of velocity reduction downstream due to net cages arranged in rows (approximately 10% reduction), hydrodynamic load results are applicable to specific cages tested as units only. A more fundamental and universal technique for load estimation on netting would provide researchers and engineers with better accuracy in modeling fish cages, which will ultimately help to build more reliable open ocean farms.

Since a net consists of cylindrical twine bars and knots similar to spheres, and there is a comprehensive body of knowledge on the fluid dynamics of cylinders and spheres, this work can be applied as a starting point.

A drag force F_D of a body with the frontal area S in steady uniform flow of velocity U, can be estimated as

$$F_D = 0.5\rho C_D S U^2 \tag{1.1}$$

where ρ is water density and C_D is the drag coefficient which is an empirically obtained function of the Reynolds number Re, a non-dimensional parameter, defined as:

$$\mathrm{Re} = \frac{Ud}{\nu} \tag{1.2}$$

where d is a dimension of a body across the flow and ν is the kinematic viscosity of the fluid. This dependence is estimated by applying dimensional analysis and

based on the fact that the force resisting motion is a sum of frictional drag caused by viscous action and pressure drag related to the shape of the object, both effects arising from the viscosity of the fluid [16].

Milne [14], Aarsnes [1] and Freedman [9] established empirical formulas for the drag coefficient of nets in steady current as a function of net geometry. Milne (equations 1.3 and 1.4) also considered the knot factor (woven or knotted net) and Aarsnes (equation 1.5) included an angle of attack:

$$C_d = 1 + 1.89S_d + 2.34S_d^2 \quad \text{for a knotted net} \tag{1.3}$$

$$C_d = 1 + 1.37S_d + 0.78S_d^2 \quad \text{for a knotless net} \tag{1.4}$$

$$C_d = 0.04 + (-0.04 + S_d - 1.24S_d^2 + 13.7S_d^3)\cos(\alpha) \tag{1.5}$$

$$C_d = 3\left(\frac{2S_d}{\mathrm{Re}}\right)^{0.07} \tag{1.6}$$

where S_d is the solidity ratio, or in other words, the ratio of actual twine area to total projected area; and α is an angle between the current direction and the net plane. The issue with the equations 1.3-1.5 is that they incorporate net solidity only, but not the Reynolds number. Milne also conducted tests to investigate marine bio-fouling effects on the drag coefficients for a range of net materials. It appears that the net drag drastically increases (up to 300%), due to fouling, even within two months of submersion. However, fouling is a further complication because it tends to both increase the solidity in the net plane and also adds material that trails out of the net plane adding further surface area.

Armour [2] studied the nature of fluid flow through woven screens. He simplified a screen with a very thin packed bed and developed a general pressure drop correlation to all types of woven and metal screens with a unique definition of the Reynolds number:

$$N_{Re} = \frac{U}{va^2 d} \tag{1.6}$$

where a is a surface area to unit volume ratio of the screen wires and d is a screen diameter.

Koo [10] developed a mathematical model for steady 2D flow around a submerged screen. The screen was replaced with a distribution of sources and then the mass and momentum balances across the screen were adjusted for this flow. The model was successfully validated with wind-tunnel tests.

Loland [12] applied the Schlichting approximation for deriving the velocity profile behind a single cylinder in steady flow and obtained a mathematical formulation for the velocity profile in the turbulent wake behind the screen, which is presented as a summation of cylinders.

In addition to current loads, nets also undergo large loads from waves. The drag force can be estimated from equation 1.1. The velocity component is presented as $|U|U$, so the direction of the force is stipulated as it changes every half a wave cycle. However, the drag coefficients in steady and oscillating flow are not the same [7]. In the meantime, there is an inertia effect due to the

acceleration of the flow in a wave. A fluid particle moving in simple harmonic motion possesses a momentum. As the fluid particle under the wave passes around the circular cylinder, it first accelerates to reach the midpoint and then decelerates down the surface. This translates to work done on the cylinder, which introduces a force on the cylinder proportional to the fluid particle acceleration and the cylinder volume [7]. This inertia force related also to the added mass, is presented in terms of an inertia coefficient C_M, another empirical, non-dimensional parameter. The interaction between drag and inertia is commonly simplified as a linear summation, known as Morison's equation, which per unit length appears as follows:

$$F = \rho C_M \frac{\pi d^2}{4} \dot{U} + \frac{1}{2} \rho C_D |U| U \tag{1.7}$$

Drag and inertia coefficients for cylinders in oscillating flow are empirically determined as functions of Reynolds number Re and Keulegan-Carpenter number KC, which is a non-dimensional drag/inertia ratio presented as

$$KC = \frac{UT}{d} \tag{1.8}$$

where T is a wave period, U is a maximum particle velocity. However, even though there have been empirical and numerical studies on net structures, a well accepted technique for deriving the inertia coefficient does not yet exist. Instead the coefficient for a circular cylinder is assumed.

The synergistic effects of current and waves on nets are assumed to be secondary. Since loads on nets in oscillating flow alone are not yet definitely quantified, the combined effects can only be minimally covered. However, [13] suggested a method to estimate the horizontal component of hydrodynamic loads on aquaculture cages exposed simultaneously to current and waves in parallel to each other. The drag equation was integrated over the projected area using a derived velocity term, representing both velocity components. However, the drag coefficient was assumed constant for each individual net wall of a cage, even though they were on different angles of attack to the flow.

The purpose of the study presented in this paper is to empirically estimate drag and inertia coefficients for scaling of quasi-static and dynamic loads on nets. In order to quantify the horizontal component of loads in current and waves at normal angles of attack, a range of plane net samples was tested in a towing tank and a wave basin at the Institute for Ocean Technology, in St. John's, NL. The data from the steady experiment was also compared with a numerical model developed by Wayne Raman-Nair, Institute for Ocean Technology, St. Johns, NL (the work has not been published yet). Based on the experimental results, a unique empirical formula for steady flow drag coefficient as a function of net solidity and circular cylinder (and sphere, in case the net is knotted) was derived. Applying a two-level factorial design [15], a synergetic effect between net solidity and current velocity was indicated. In the end, unsteady flow drag

coefficient was formulated as a function of particle velocity and net porosity; and added mass was estimated through effective thickness (the width of water that is conjectured to be affected by the net), which is a function of wave frequency and net solidity.

II. Experimental Program

2.1 Net samples

Experiments were conducted on plane net samples alone as the simplest possible case. Five net samples, 1 sq. meter in area each, (Table 2.1) were tested. All samples, except one, were from the same material (nylon). Nylon is currently the most commonly used net material in the aquaculture industry. Although net material is conjectured to have a relatively small effect on total hydrodynamic load, testing the same material minimizes errors due to changes in material. The aquaculture industry maintains two major types of mesh shapes: diamond and square. To diminish the effects of individual twine bar orientation, all samples used were square shaped.

Table 2.1 Net sample geometry
* D knot shape was approximated as a sphere
** MM –manual measurements
*** IA – image analysis

Sample	Material	Knot factor	Twine diameter	Knot diameter	Mesh	Solidity (MM)**	Solidity (IA)***
			d	D*	l	Sd	Sd
			mm	mm	mm		
1	nylon	woven	3.0		77.8	0.077	
2	polyethylene	knot	3.2	10.2	80.3	0.095	
3	nylon	knot	1.0	2.3	22.2	0.099	0.089
4	nylon	woven	0.9		10.1	0.178	0.185
5	nylon	woven	2.0		16.1	0.249	

Solidity S_d is the ratio of actual twine area to total projected area; it is defined as follows:

$$S_d = 2\frac{d}{l} \text{ for woven (knotless) nets} \tag{2.1}$$

$$S_d = \frac{2ld + \pi D^2/4}{l^2} \text{ for knotted nets} \tag{2.2}$$

The first component of the numerator in equation 2.2 should strictly be $2(l-D)d$, but extra twine is included to account for the convexity of the knots. The mesh geometry is specified on Fig 2.1.

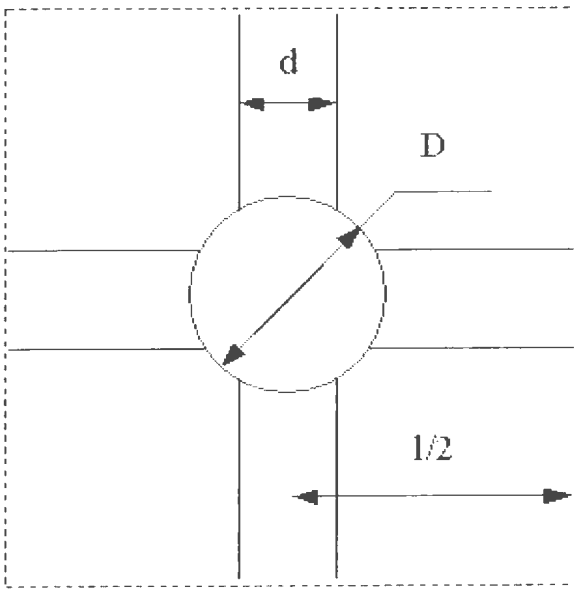

Fig. 2.1 Knotted net mesh geometry specification.

Manual measurements, using a vernier caliper and a micrometer screw gauge, of net geometry are subject to errors in measurement on small elements, which are then multiplied over larger areas. In order to check the accuracy of manual measurements, image analysis was employed to quantify the frontal area of the net samples. Image analysis is a software-based technique to measure objects from an image. A photo image of the net sample was taken on a contrasting background and the image was converted into a grayscale image. Then, setting a grayscale threshold, the image was ranged into two levels only: black and white. Applying a Matlab code, each pixel was perceived as a member of a matrix, so an amount of black or white pixels can be counted and thus the actual twine area is estimated. It can be seen from Table 2.1 that image analysis and manual measurement results are approximately 10% different. The agreement might change with different lighting conditions. In the present case, unequally distributed light over the sample caused some shadows. This problem was more evident in images of large mesh samples. For small mesh cases, a smaller image of a sample could be taken and then multiplied by the total projected area with small error (this was actually done), but for nets with large meshes, the amount of twine in a small image segment when linearly multiplied to the larger area of the actual sample may cause a significant error. Also light on objects may show as larger pixel areas than in reality if the light is reflected from the lines.

2.2. Hydrodynamic loads measuring apparatus

A specially designed apparatus was used for the load measurements (Fig. 2.2-2.5). A net sample was hung between two metal bars, each suspended on springs and restrained by a load cell. The load cell and spring suspension were grounded to a metal support frame. The entire construction was supported on a towing carriage. In order to reduce the hydrodynamic load on the bars supporting the net, half-ellipse shrouds were fitted around the bars and anchored to the support frame. The net was well submerged (0.5m) so surface turbulence did not impact the net drag. To prevent the horizontal edges of a net sample from flapping, top and bottom meshes were strung on 3mm diameter rods (Fig. 2.5).

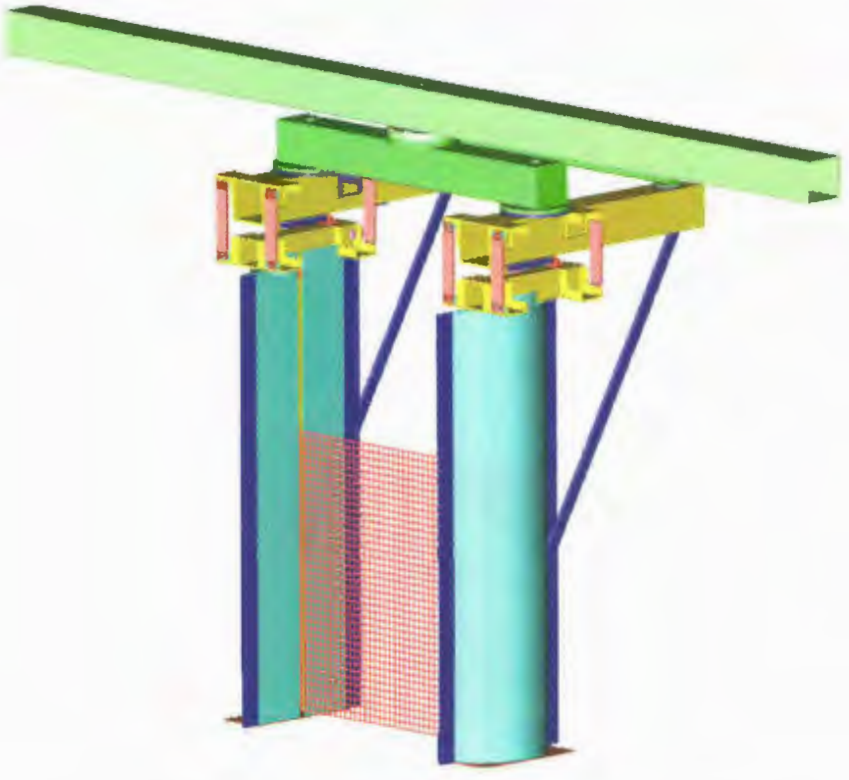

Fig. 2.2 The 3D sketch of the load measuring apparatus

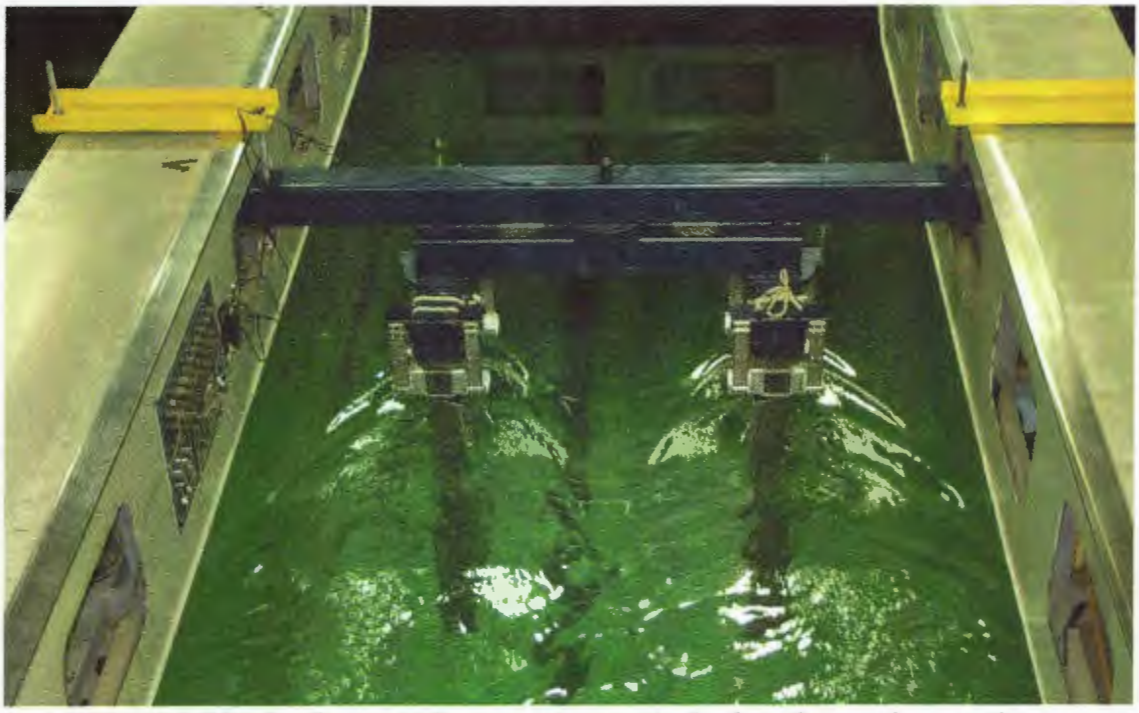

Fig. 2.3 The load measuring apparatus attached to the towing carriage

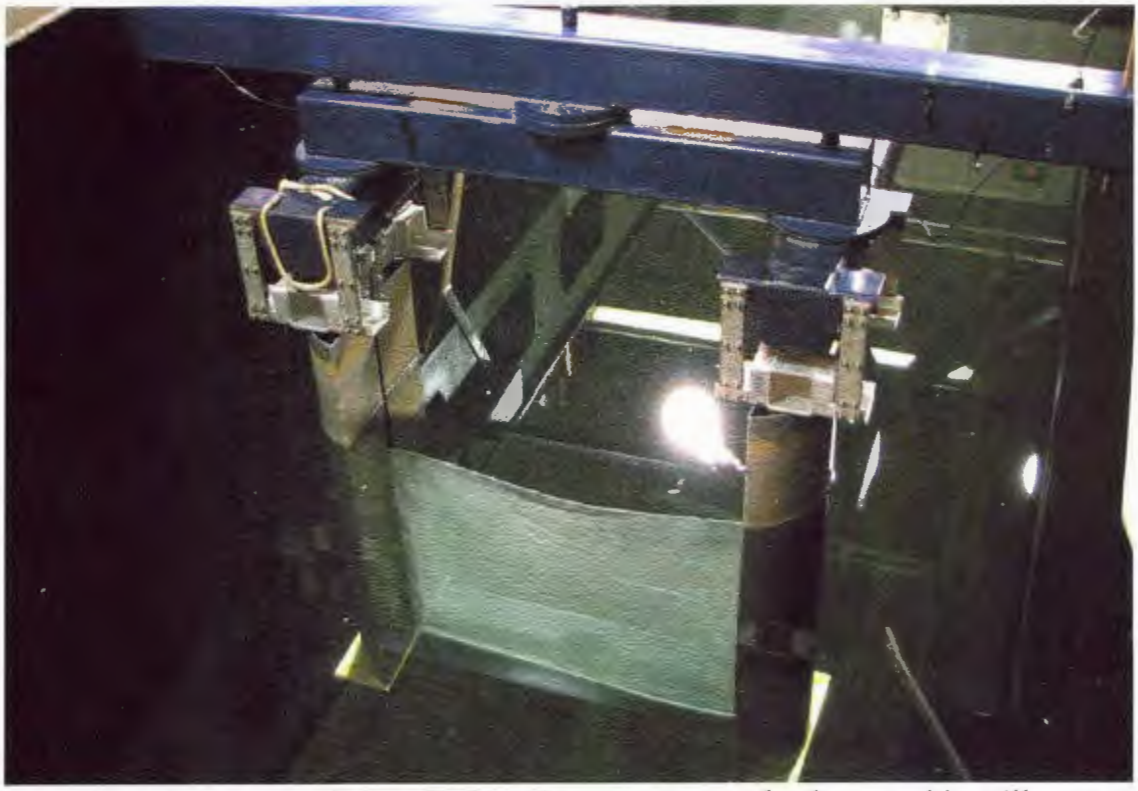

Fig. 2.4 The net sample installed on the apparatus and submerged in still water

Fig. 2.5 The net sample towed

From Fig 2.5 it can be clearly seen that the net distorts. The scale effect of distortion is assumed to be negligible.

2.3 Steady flow experiment

The steady flow drag experiment was conducted in a tow tank of two-meter depth. Each net sample was tested twice in a flow normal to the plane of the net at the following velocities: 0.1, 0.2, 0.5, 0.75, 1.0, 1.25, 1.50, 2.0 m/s. In real environmental settings, net structures might undergo loads from higher currents; however, in the experiment, the apparatus started to experience significant vibration at higher speeds. To avoid significant noise in the data caused by vibration tests were not done above 2 m/s, which is approximately 4 knots.

2.4. Oscillating flow experiment

The in-wave experiment was performed in a wave basin of two-meter depth (Fig 2.6). Each net sample was tested in eight different sets of waves (Table 2.2).

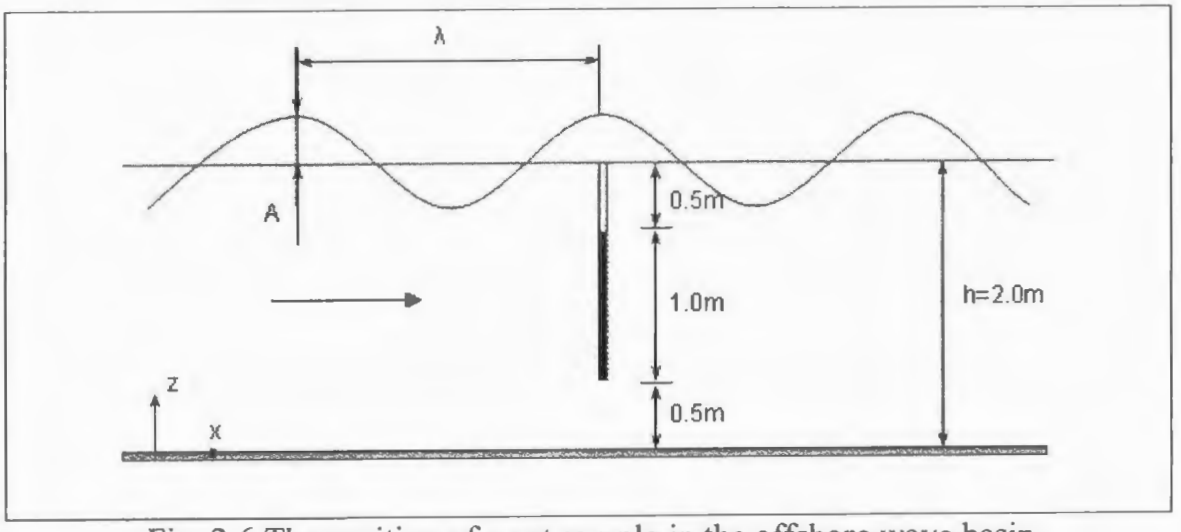

Fig. 2.6 The position of a net sample in the offshore wave basin

The wave amplitude for each trial was determined by wave-maker capability to maintain steady amplitude for a chosen wavelength. A wave probe was installed upstream of the experimental apparatus to record wave profiles. In the process of data filtration, sinusoidal fits were superimposed to determine steady-state wave amplitude and wave frequency for each run. Waves of a length less than or equal to the water depth are considered to be deep-water waves. The wavelength and frequency of deep water waves have the following dependence:

$$\lambda = \frac{2\pi g}{\omega^2} \tag{2.1}$$

If the wavelength is greater than the water depth, the wavelength and frequency are more precisely related by the dispersion relationship:

$$\omega = (kg \tanh(kh))^{1/2} \tag{2.2}$$

where k is the wave number and is equal to $2\pi/\lambda$, g is the gravitational acceleration and h is the water depth. As can be seen from equation 2.2, the wavelength cannot be explicitly expressed in terms of the wave frequency, so an iterative method is applied to estimate exact wavelength for each run.

Table 2.2 Wave parameters

Wave length λ, m	Wave amplitude A, m	Quantitative depth criteria h/ λ	Qualitative depth criteria	Wave frequency ω, rad/sec
2	0.03	1.00	deep	5.55
4	0.07	0.50	shallow	3.92
6	0.10	0.33	shallow	3.16
8	0.16	0.25	shallow	2.66
10.2	0.18	0.20	shallow	2.26
12.4	0.15	0.16	shallow	1.96
15.4	0.13	0.13	shallow	1.64
20.5	0.11	0.10	shallow	1.28

A velocity probe was also installed at a depth of 1 meter to record the horizontal water particle velocity.

In both experiments, loads in calm water were measured and "no-net" runs were conducted for all towing velocities and sets of waves to deduct offsets

arising from the small loads applied on the horizontal rods. After each run a proper amount of time (approximately 20 min) was allotted for the tank water to stabilize prior to the next run.

2.5 Data filtration

To filter out noise or spurious signals in the data output from the probes and load cells, Igor data analysis software was used.

For the steady flow experiment, moving averages of force and towing velocities were calculated.

For the oscillating flow, first a segment of a stabilized wave profile was chosen and a sinusoidal fit was overlaid to estimate steady state wave amplitude and frequency. Afterwards, by applying the frequency estimated from the wave profile in order to be consistent, the horizontal force and horizontal particle velocity profiles (Fig. 2.8 and 2.9) were fitted with sinusoids to determine the maximum horizontal force and velocity respectively as well as their phase shifts (from this point in the text, force, velocity and acceleration imply the horizontal components only, unless specified otherwise). The velocity profile was differentiated to determine maximum particle acceleration and its phase shift (Fig 2.10). A Fourier analysis of the force signal was also performed (Fig. 2.11) to compare the actual force frequency with imposed wave frequency. The difference was less than 2%.

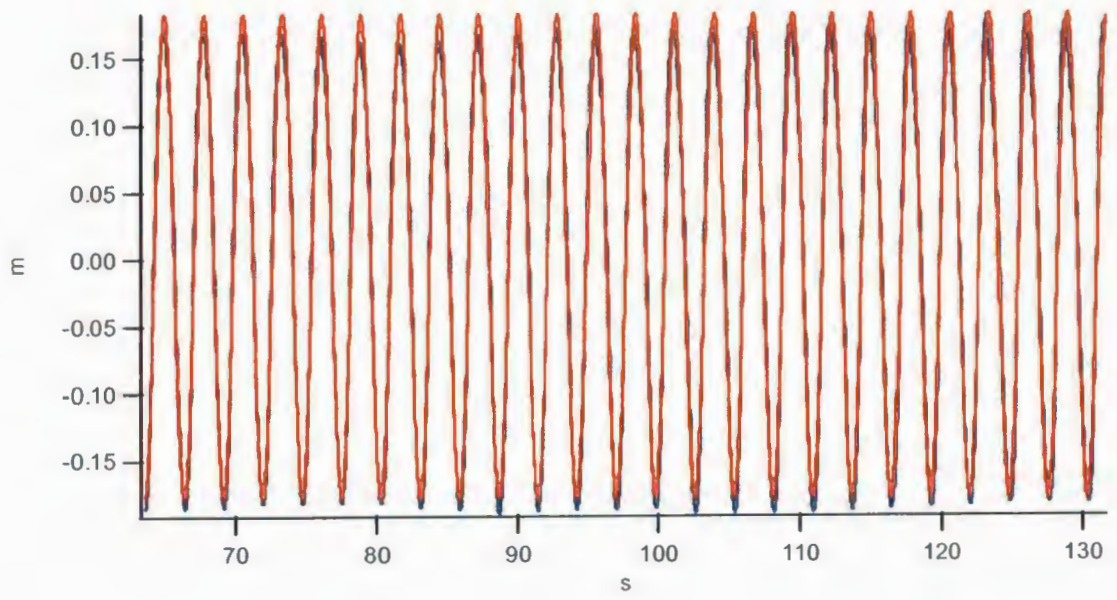

Fig. 2.7 Wave profile (blue) and sinusoidal fit (red)

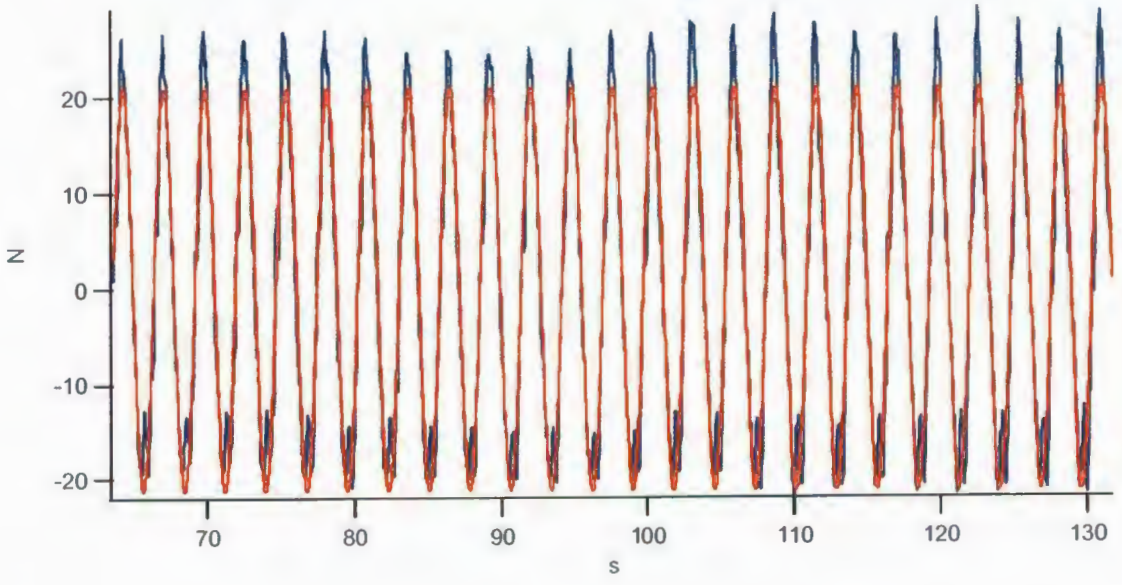

Fig. 2.8 Horizontal force profile (blue) and sinusoidal fit (red)

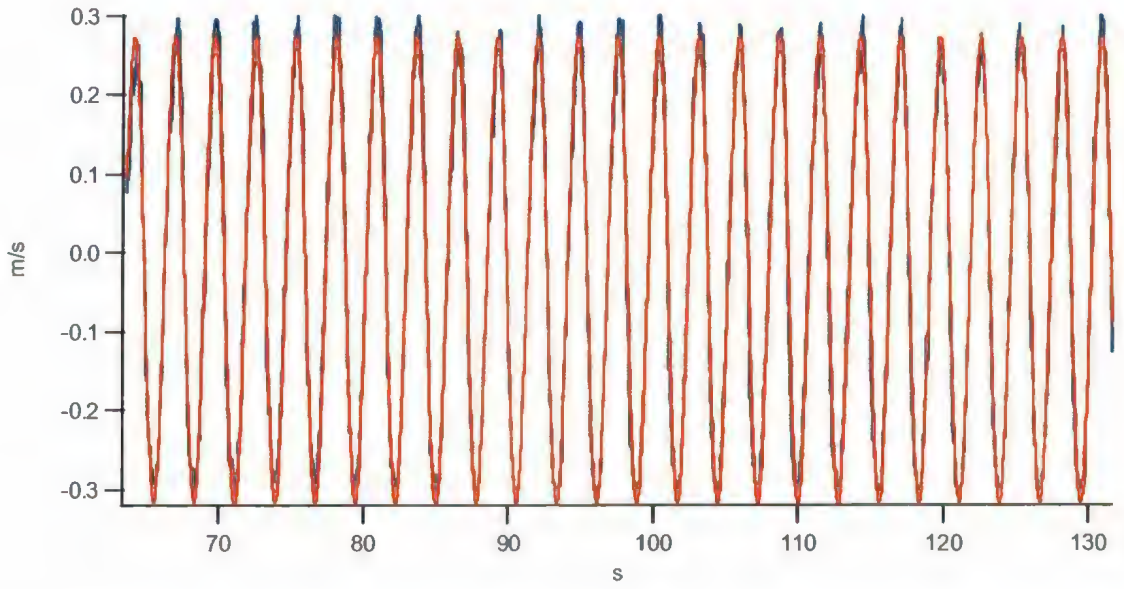

Fig. 2.9 Maximum (at water surface) horizontal particle velocity profile (blue) and sinusoidal fit (red)

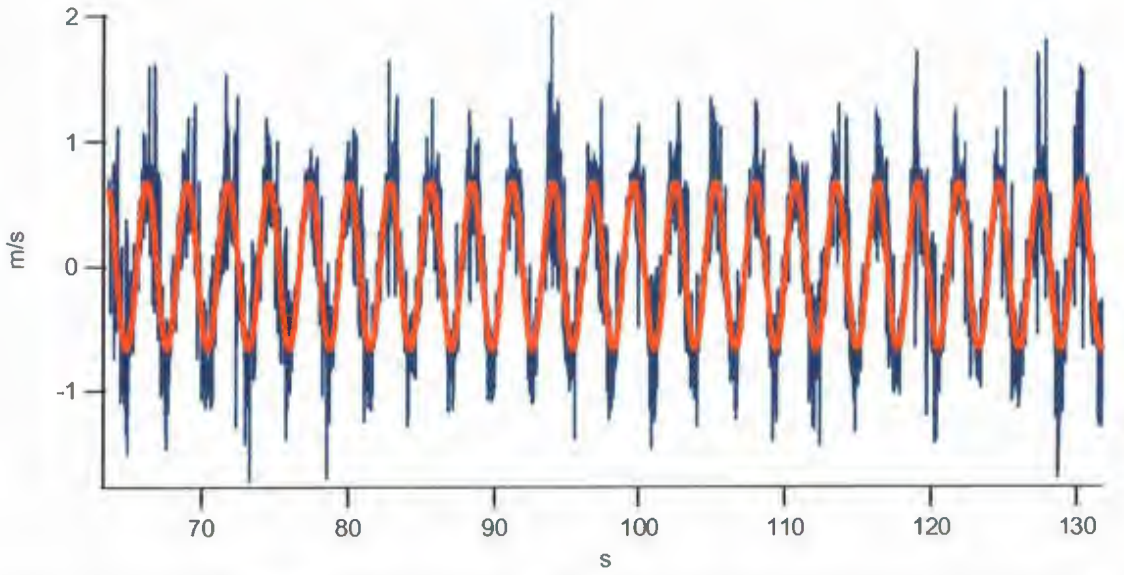

Fig. 2.10 A differentiated profile of horizontal particle velocity profile (blue) and sinusoidal fit (red)

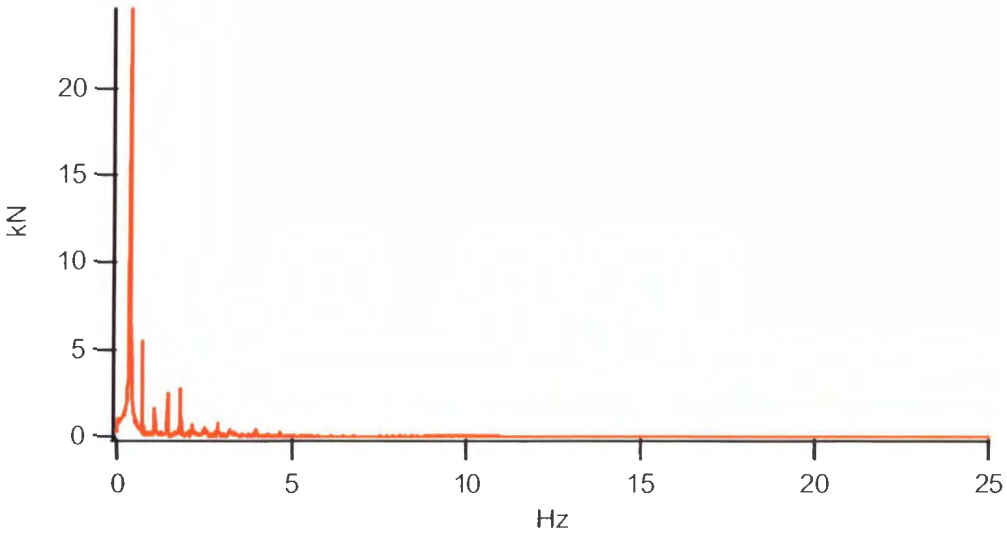

Fig. 2.11 Fourier analysis of force

It can be observed visually (Fig 2.12) and further verified by the Fourier analysis (Fig. 2.13) that the higher wave frequency cases (2.26-5-55 rad/sec, or 2-8 m wave length) were dominated with ringing caused by natural vibration in the apparatus or the towing carriage. This ringing probably occurred because the net was not heavily or uniformly loaded, since there was a significant difference between the particle velocity on the surface and on the bottom of the net. Thus, the data from these runs was noisy and was not considered for further data analysis.

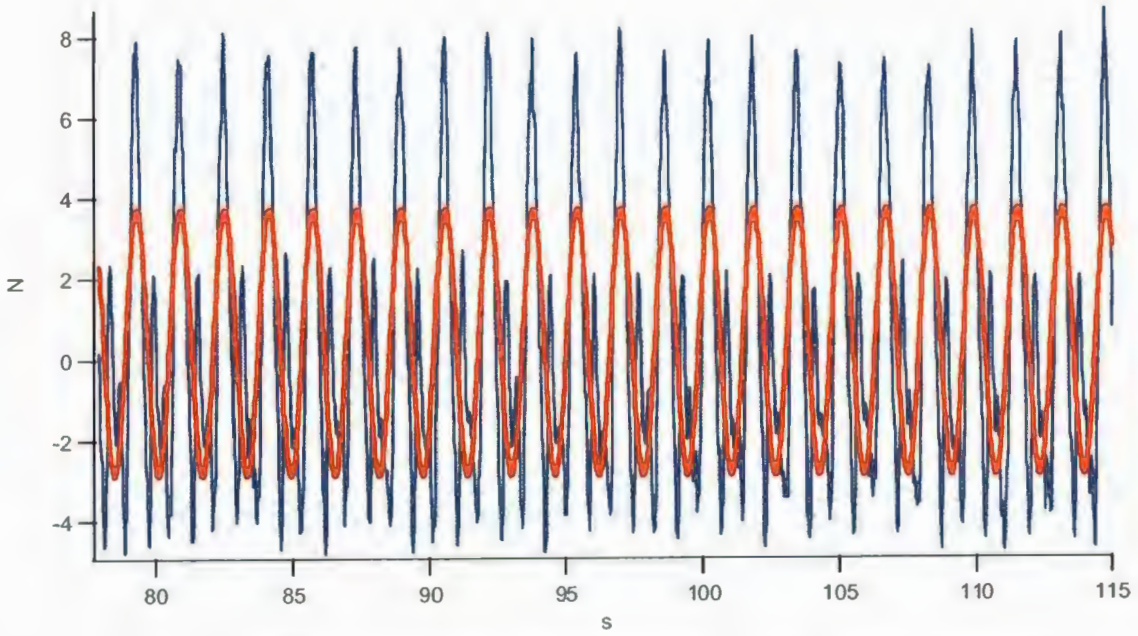

Fig. 2.12 Force profile (blue) and sinusoidal fit (red), noisy example

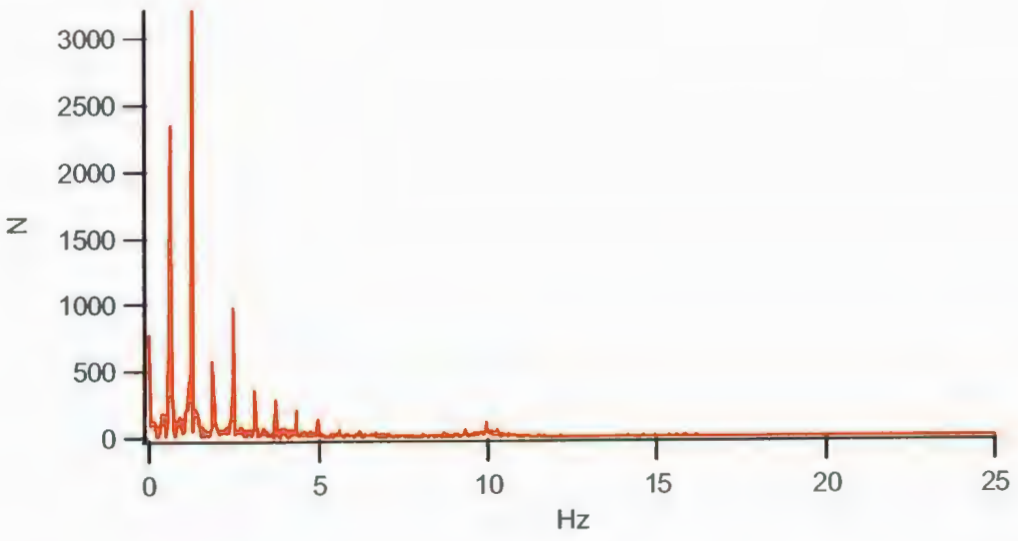

Fig. 2.13 Fourier analysis of force, noisy example

III. Discussion of results

3.1 Drag force in steady flow

3.1.1 Gross drag coefficient comparison with existing empirical formulae

It has been mentioned that Milne [14], Aarsnes [1] and Freedman [9] established empirical formulae for estimating the drag coefficient in steady flow.

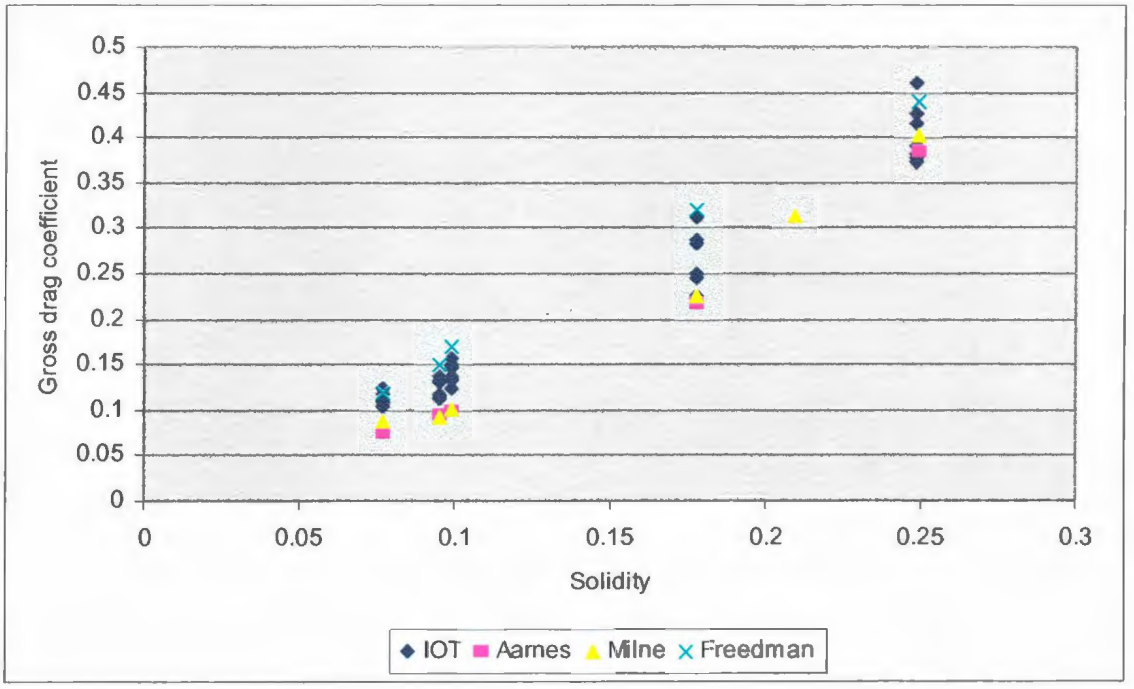

Fig. 3.1 The comparison of the gross drag coefficient for net samples tested in the experiment with empirical formulae derived by Aarnes and Milne.

Fig. 3.1 demonstrates the comparison of the present experimental results with these formulae in terms of gross drag coefficient, which is drag coefficient per total twine area. As total projected area of net samples is 1 square meter in the experiment, solidity equals to actual twine area.

Overall, the present experimental data are in good agreement with all existing formulae, especially with the Freedman formulae, which incorporates the Reynolds number and hereby more reliable. However, it should be mentioned that the difference with Aarnes and Milne formulae might have been caused by slightly increased water velocity in the net plane due to flow around the shrouds of the load measuring apparatus.

3.1.2 Synergistic effect of net solidity and current velocity

The drag force is a function of current velocity and net geometry. Fig. 3.2 clearly illustrates this dependence. In addition, it can be seen that velocity and solidity have a synergistic effect on the drag; in other words, their combined effect has a non-linear nature.

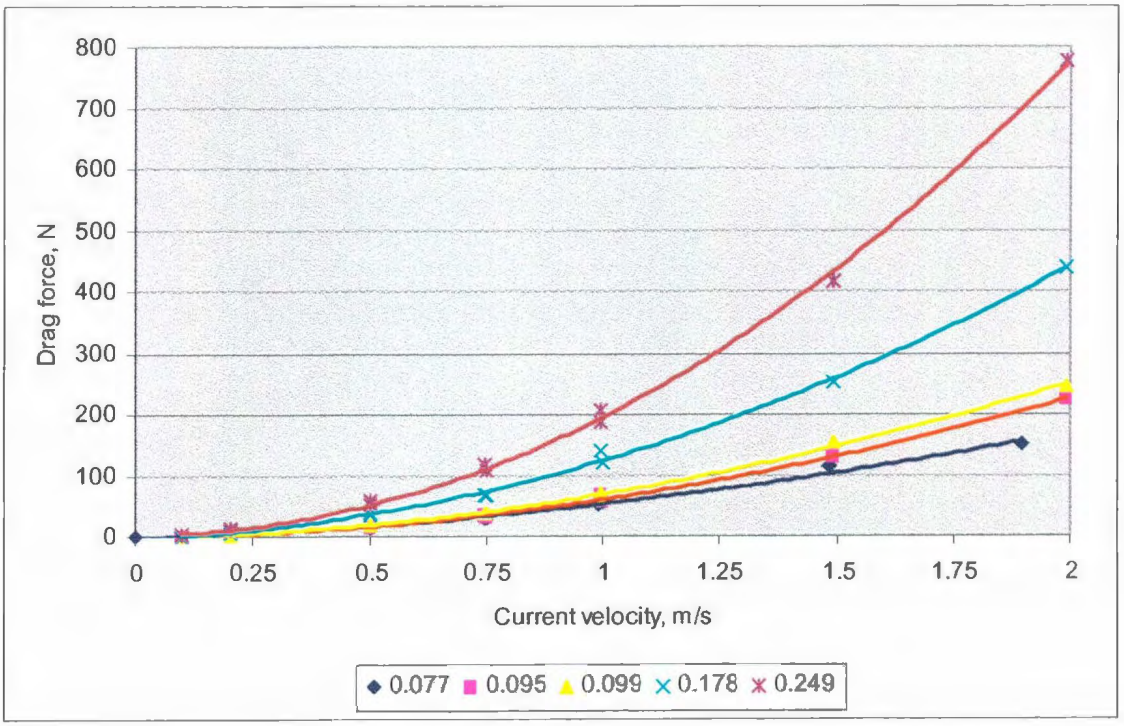

Fig. 3.2 Drag force vs. current velocity for net samples of different solidities

To verify this synergistic effect, a two-factorial experimental design [15] analysis was applied. The two-factorial design screens effects and interaction effects of factors on a desired parameter. Each chosen factor (solidity as factor A and velocity as factor B here) was assigned two levels (i.e. 0.5 and 2.0 m/s for current velocity) and an output (drag force, in particular) was estimated for each

combination of factors and their levels. The analysis of variances (ANOVA) was then conducted to identify significant factors. The ANOVA and interaction graph (Fig 3.3) illustrate that the interaction effect of solidity and velocity significantly impact the drag.

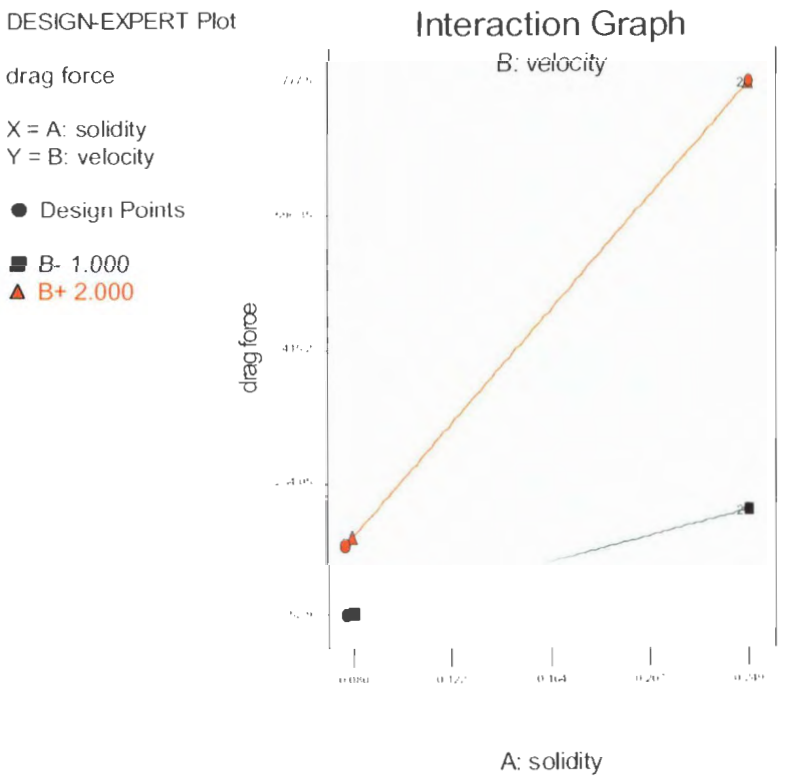

Fig. 3.3 Interaction effect of net solidity and current velocity

Fig. 3.3 clearly shows the "positive" effects of solidity and velocity on the drag: as solidity or velocity increases, the drag also increases. In other words, these factors combined have a larger effect on the drag than just a linear summation of the two effects. This compound interaction can be explained by the

increasing interaction of flow around individual twine bars as these bars get closer and closer to each other.

3.1.3 Drag coefficient: comparison of experimental and numerical results

Dr. Wayne Raman-Nair from the Institute for Ocean Technology, NRC, St. John's, NL has developed a numerical model to estimate loads on plane nets (the work has not been published yet).

The model was developed in the Matlab software environment. The model perceives every twine bar as a spring with masses lumped on the end points. Fig 3.4 and 3.5 compare the present experimental data with numerical model results for two chosen samples (with low and high solidity, knotted and knotless respectively) over a range of current velocity.

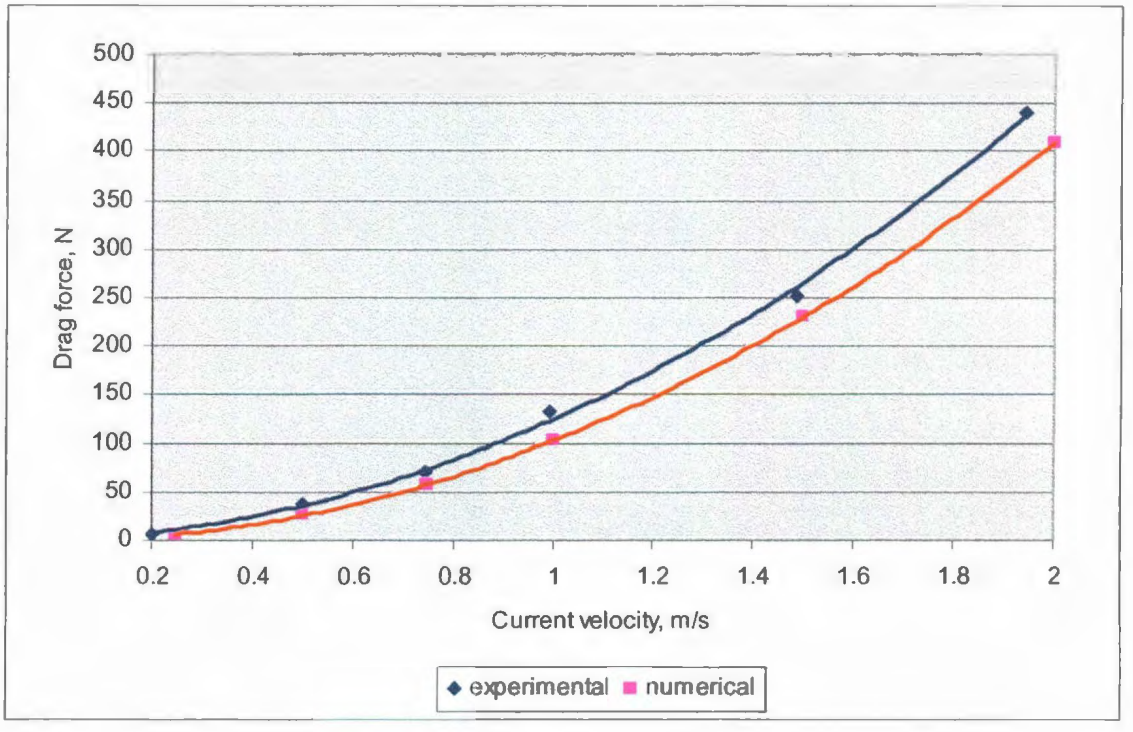

Fig. 3.4 The comparison of experimental and numerical results for the sample with solidity of 0.095

Overall, there is good agreement between the experimental results and the corresponding numerical simulations. As mentioned before, the experimental data might slightly over-predict the drag load due to increased velocity generated by the apparatus fairings (shrouds); however, this is unlikely to be the case as the drag produced by fairings was accounted in "no-net" runs.

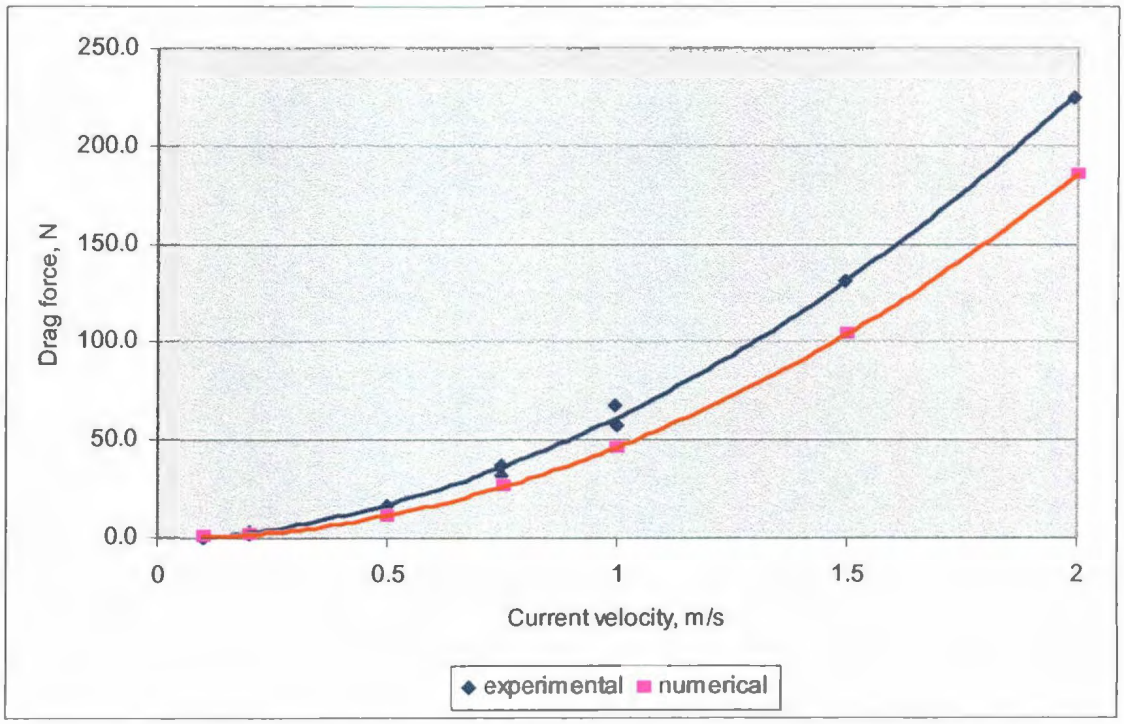

Fig. 3.5 The comparison of experimental and numerical results for the sample with solidity of 0.178

3.1.4 A universal formula for net drag coefficient estimation

The experimentally obtained drag coefficients for nets were plotted against Reynolds number for each sample and compared with the drag coefficient curve for the circular cylinder with the same diameter as the twine diameter (Fig. 3.7-3.11). The drag coefficient for nets has an obvious correlation with the drag coefficient of a circular cylinder: the curves for nets and the cylinder are "parallel" with a pronounced and consistent offset.

The total force on a knotted net per projected area measured in the experiment was expressed as:

$$C_{D[mesh]} = \frac{F/(2ld + \pi D^2/4)}{0.5\rho U^2} \tag{3.1}$$

From the force balance:

$$F = F_{cyl} + F_{sp} \tag{3.2}$$

where F_{cyl} is the load on two twine bars (cylinders) forming a mesh cell and F_{sp} is a load on a knot, simplified as a sphere.

As the net is a system of individual independent cylinders that are interconnected with each other forming a screen, the stream flow has to accelerate to go through the reduced area and then decelerate as it exits the mesh. The downstream velocity is known to be lower than the upstream velocity and thus the velocity losses (or energy losses) in the mesh, appear as drag. Blevins [3]

relates the increased velocity (local velocity around individual bars) to the screen porosity:

$$U' = \frac{U}{1 - S_d} \tag{3.3}$$

where U is local velocity, U is a stream velocity and $(1\text{-}S_d)$ is net porosity, which is the ratio of "twine free" area to total projected area ($\frac{l^2 - 2ld}{l^2}$). As can be seen, net solidity and porosity are interchangeable, so both parameters are used further in the text. Thus equation 3.2 can be expanded as:

$$F = \frac{1}{2}\rho[C_{D[cyl]}2ld + C_{D[sp]}\frac{\pi d^2}{4}]\frac{U'^2}{(1 - S_d)^2} \tag{3.4}$$

Substituting (3.4) into (3.1) yields:

$$C_{D[net]} = \frac{[C_{D[cyl]} + C_{D[sp]}]}{(1 - S_d)^2}\frac{\frac{\pi}{8}\alpha\beta}{(1 + \frac{\pi}{8}\alpha\beta)} \tag{3.5}$$

where $\alpha = \frac{D}{l}$ and $\beta = \frac{D}{d}$

Drag coefficients for circular cylinders and spheres have been extensively studied and can be reliably estimated as [17]

$$C_{D[cyl]} = 1 + \frac{10}{\mathrm{Re}^{2/3}} \tag{3.6}$$

$$C_{D[sp]} = \frac{24}{\mathrm{Re}} + \frac{6}{1 + \mathrm{Re}^{1/2}} + 0.4 \tag{3.7}$$

The Reynolds number in equations (3.6) and (3.7) was taken for local velocity as specified in equation (3.3). The Reynolds number for the drag coefficient of the sphere can be modified as follows:

$$\mathrm{Re}_{sp} = \frac{Ud}{\nu(1-S_d)}\frac{D}{d} = \mathrm{Re}_{cyl}\frac{D}{d} \tag{3.8}$$

For nets without knots (3.5) is simplified as:

$$C_{D[net]} = \frac{C_{D[cyl]}}{(1-S_d)^2} \tag{3.9}$$

Using (3.5) and (3.9) the drag coefficient was estimated for all solidities and current velocities. The results were plotted vs. the Reynolds number and compared with those obtained empirically. The analytical model initially appeared to only sporadically match the experimental results. However, more thorough observation led to a supposition that the net porosity had a more complex influence on the stream velocity than that published by Blevins (1984). Thus, equations 3.5 and 3.9 were corrected to match the empirical results (Fig. 3.8-3.12) and the analytical model was adjusted as follows:

$$C_{D[net]} = \frac{[C_{D[cyl]} + C_{D[sp]}]}{(1-S_d)^n}\frac{\frac{\pi}{8}\alpha\beta}{(1+\frac{\pi}{8}\alpha\beta)} \tag{3.10}$$

$$C_{D[net]} = \frac{C_{D[cyl]}}{(1-S_d)^n} \tag{3.11}$$

where n is a function of the net solidity and the function can be approximated as (Fig. 3.6):

$$n = 0.423 S_d^{-0.82} \tag{3.12}$$

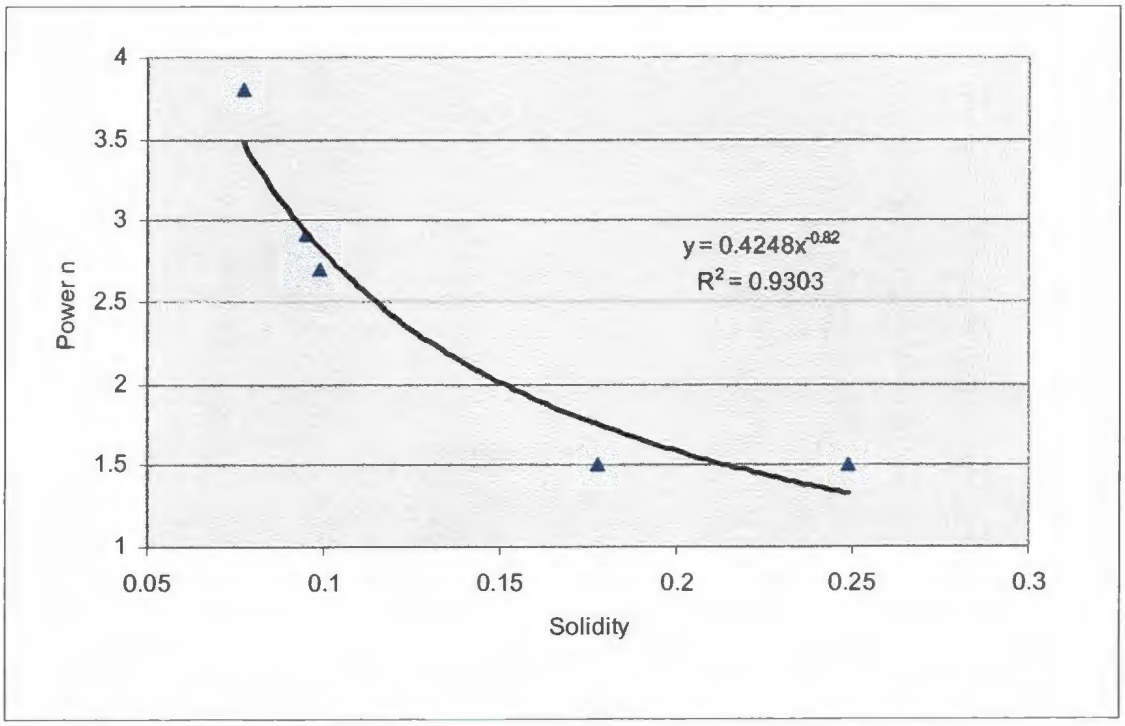

Fig. 3.6 The estimation of the power n for the model as a function of the net solidity

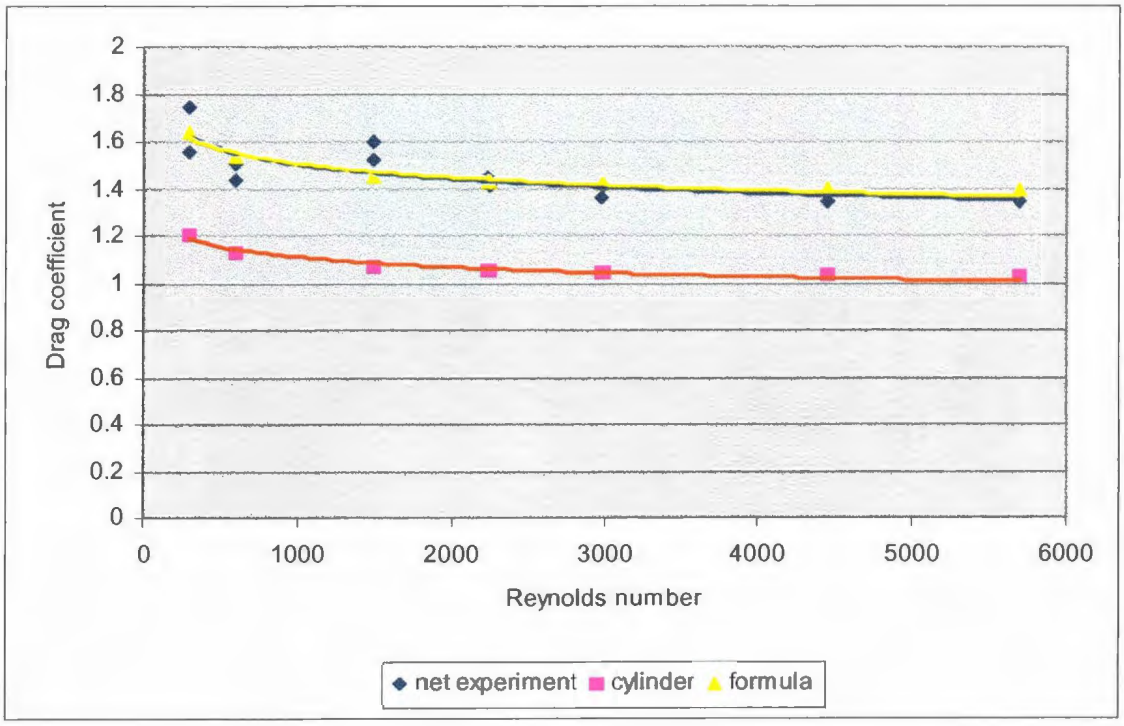

Fig. 3.7 The drag coefficient vs. the Reynolds number. Sample 1, S_d=0.077

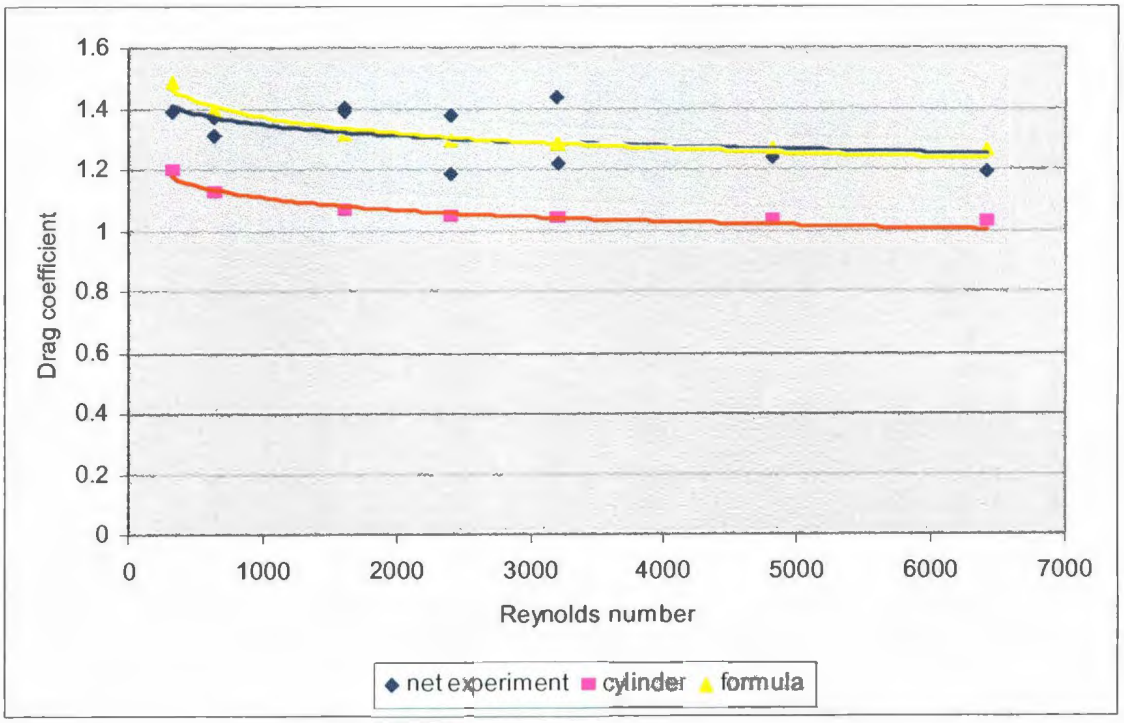

Fig. 3.8 The drag coefficient vs. the Reynolds number. Sample 2, S_d=0.095

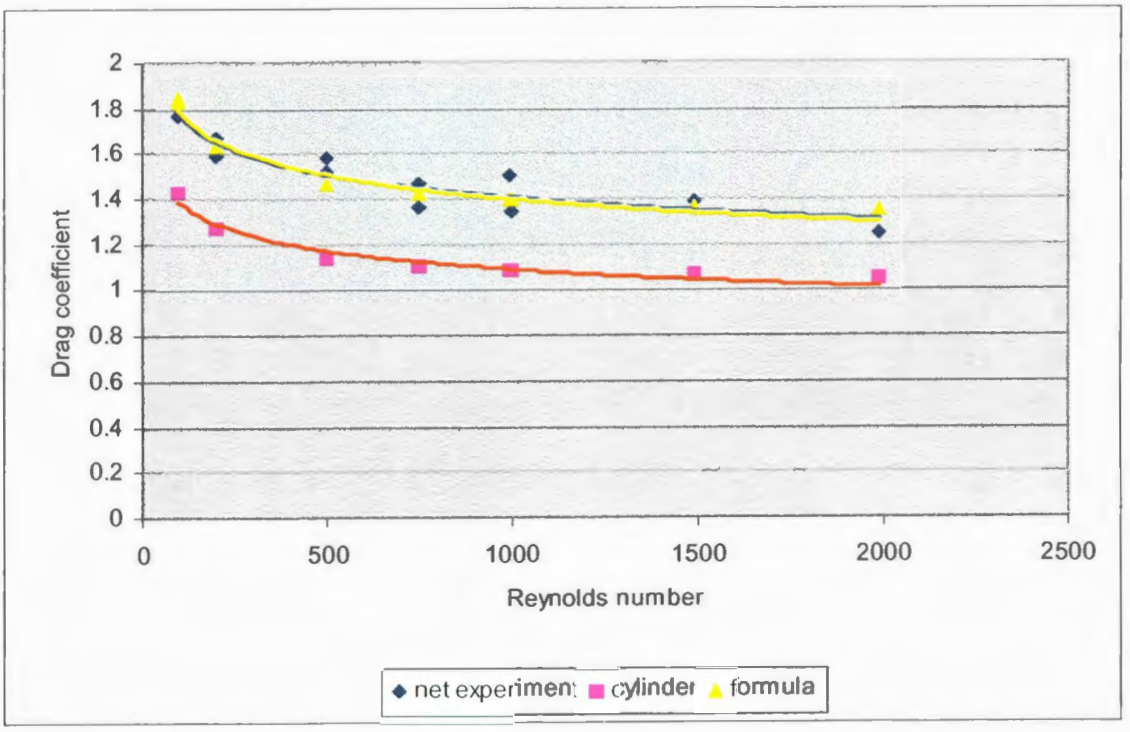

Fig. 3.9 The drag coefficient vs. the Reynolds number. Sample 3, S_d=0.099

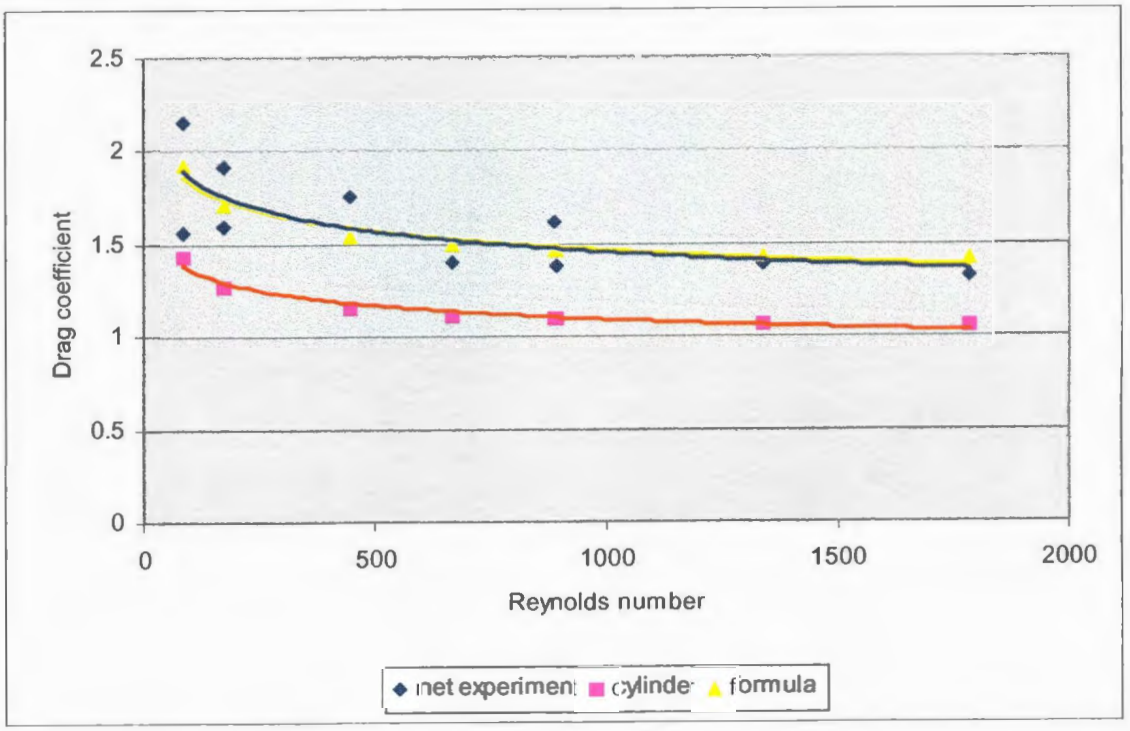

Fig. 3.10 The drag coefficient vs. the Reynolds number. Sample 4, S_d=0.178

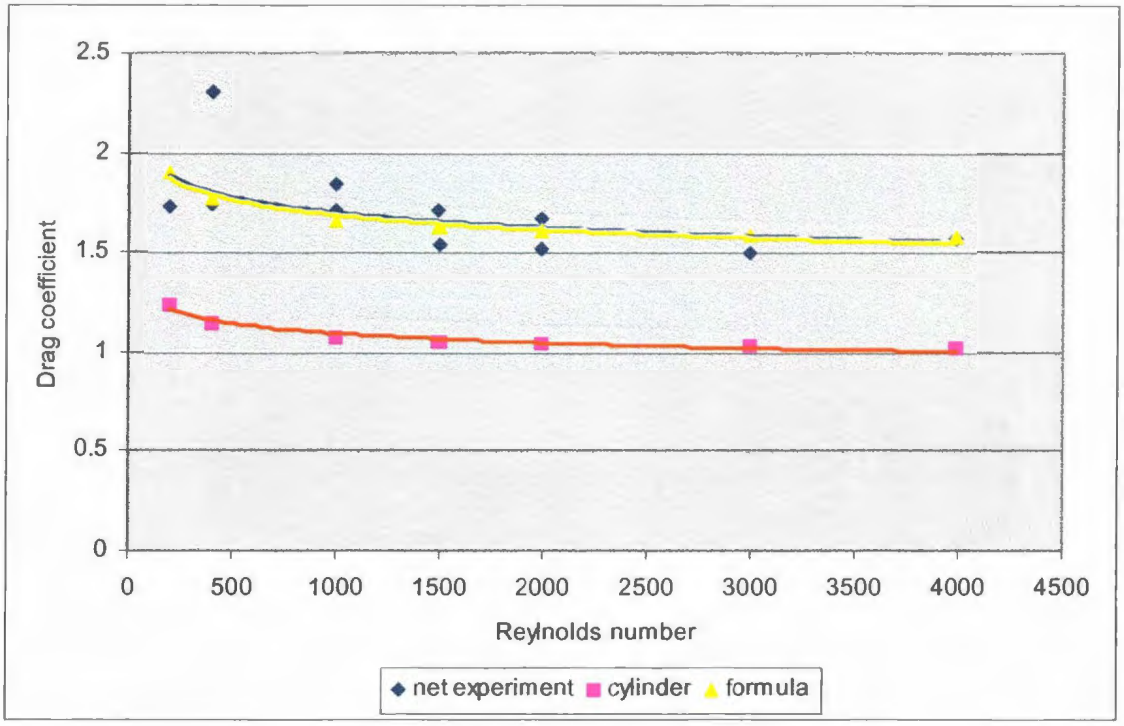

Fig. 3.11 The drag coefficient vs. the Reynolds number. Sample 5, S_d=0.249

The suggested model for the steady drag estimation is developed to match the empirical data and provides a quantification of the effect of solidity in influencing the drag coefficient of net structures. In the meantime, equation 3.3 is an approximation of the local fluid velocity and relying on the experimental results it can be improved as:

$$\tilde{U} = \frac{U}{(1 - S_d)^{n/2}} \tag{3.13}$$

The advantage of the suggested formulae (the equations 3.10 and 3.11) is that they incorporate the drag coefficient of cylinder and sphere and thus include fluid conditions through the Reynolds number, unlike the formulae of Aarnes and

Milne, which incorporate net solidity only. The formulae may also be able to be applied for different angle of attacks as it includes the drag coefficient of cylinder and sphere. This however would be subject to further verification. The dependence of the data on the cylinder might also assist in further investigation of flow through nets.

3.2 Drag force and added mass

3.2.1 Estimation form the total wave force in oscillating flow

For the last four sets of waves, in which the signals were relatively clean and noise-free, the drag component and added mass were extracted from the total wave force by applying a vector approach (Fig. 3.12).

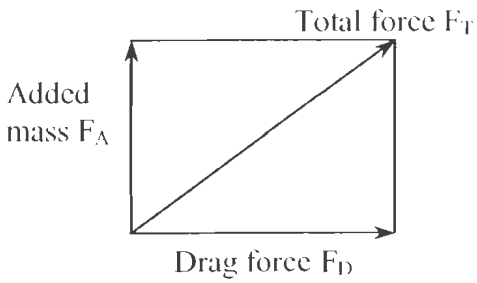

Fig. 3.12 Vector breakdown for maximum drag force and added mass

The total horizontal force on the net sample was taken to be a steady state sinusoid, which can be expressed as a vector and resolved into two components, one in phase with the horizontal wave particle velocity and one in phase with the horizontal wave particle acceleration. The velocity and the drag force, which is a function of the velocity, are taken to be in the same phase. Similarly the acceleration and the added mass are taken to be in the same phase, which is 90 degrees (orthogonal) to the phase of the velocity and drag. Thus:

$$F_D = F_T \sin(wt + \varphi_v) \tag{3.14}$$

$$F_A = F_T \sin(wt + \varphi_a) \tag{3.15}$$

where

F_d - drag force

F_A added mass

F_T - total wave force

ω wave frequency

φ_u velocity phase

φ_a acceleration phase

As the wave amplitude was much smaller than the water depth, the ratio of wave amplitude to wavelength did not exceed 1/20. Also the basin floor was flat, and thus it is reasonable to assume Airy linear wave theory to compare the velocity measured in the experiment with analytical predictions. According to the Airy wave theory, velocity and acceleration can be estimated as:

$$u = A\omega \frac{\cosh(kz)}{\sinh(kh)} \cos\theta \tag{3.16}$$

$$\frac{\partial u}{\partial t} = A\omega^2 \frac{\cosh(kz)}{\sinh(kh)} \sin\theta \tag{3.17}$$

where h is water depth, θ kx-ωt; x and z are axis specified on Fig. 2.5

It can be assumed that maximum velocity U_{max} is at x=o at a point of time equals zero, so $\cos\theta$ 1. As the velocity and acceleration have a 90 degrees phase shift, θ 90^0 for acceleration and consequently $\sin\theta$=1. Overall, experimental and analytical results are in good agreement (Appendix II).

As mentioned previously, the particle velocity was measured with the probe at a depth of 1 meter. However, the force measured with the load cells represented an integrated average over the net sample. In order to adequately compare drag and added mass versus water particle velocity and acceleration respectively, measured velocity and consequently acceleration had to be correlated to an integrated average over the area of the net sample.

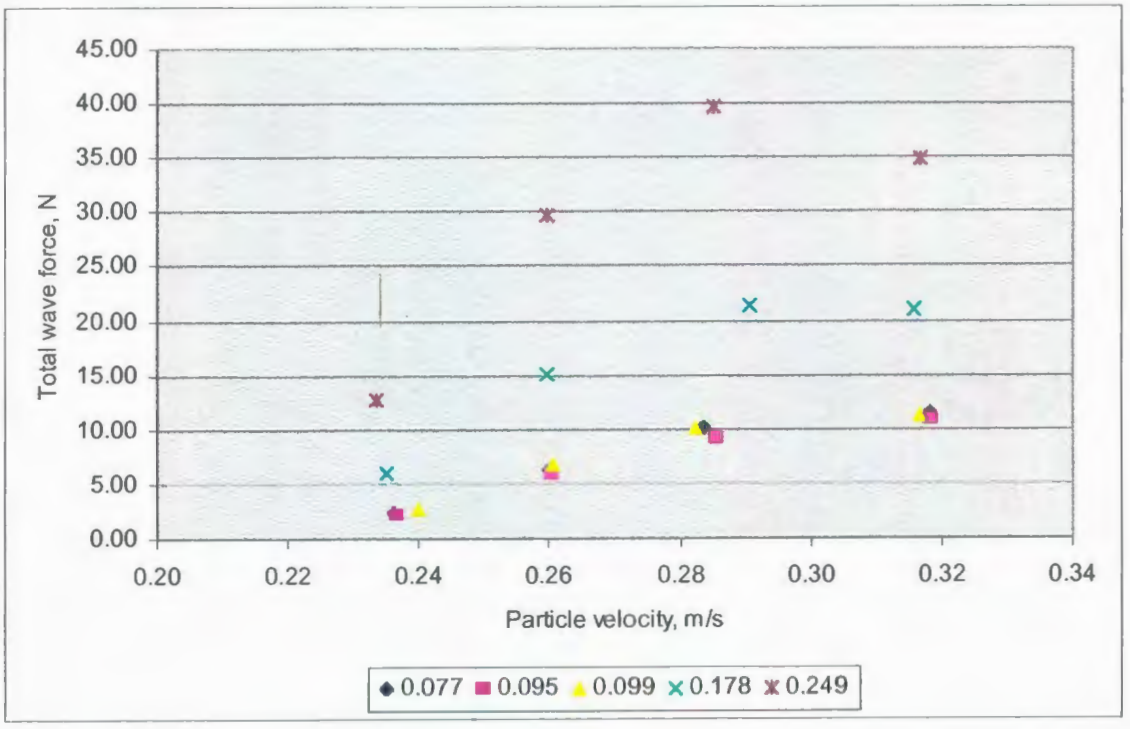

Fig. 3.13 Total wave force vs. particle velocity for five samples of different solidities (the legend presents quantitative solidity)

To estimate integrated averages for velocity and acceleration, equations 3.16 and 3.17 were integrated with respect to z over the net.

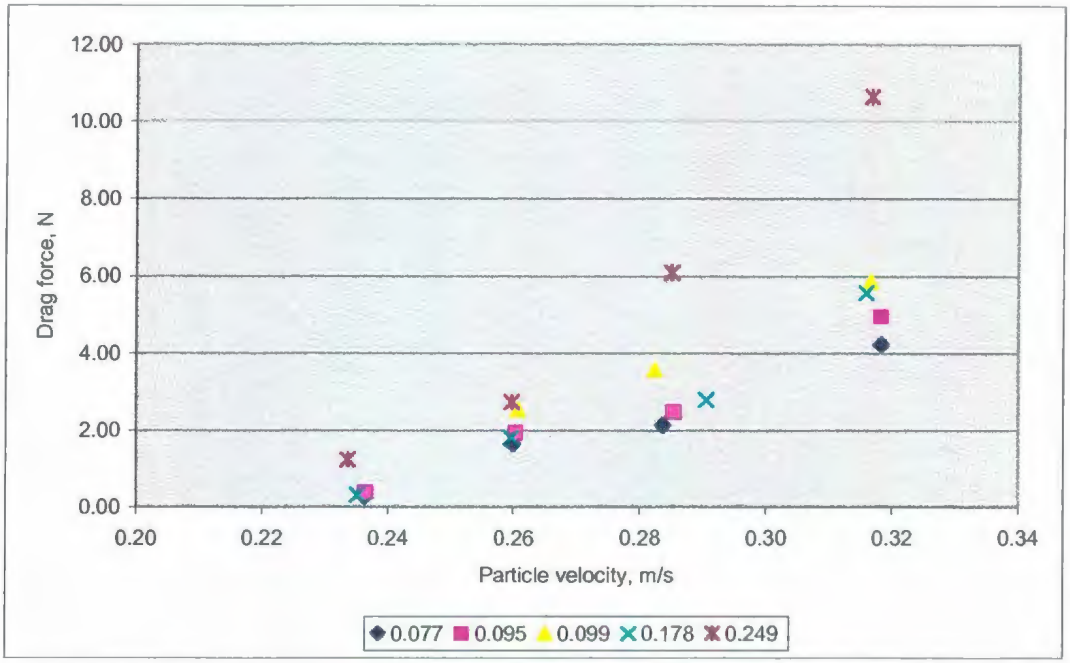

Fig. 3.14 The drag component of the total wave force vs. particle velocity for five samples of different solidities (the legend presents quantitative solidity)

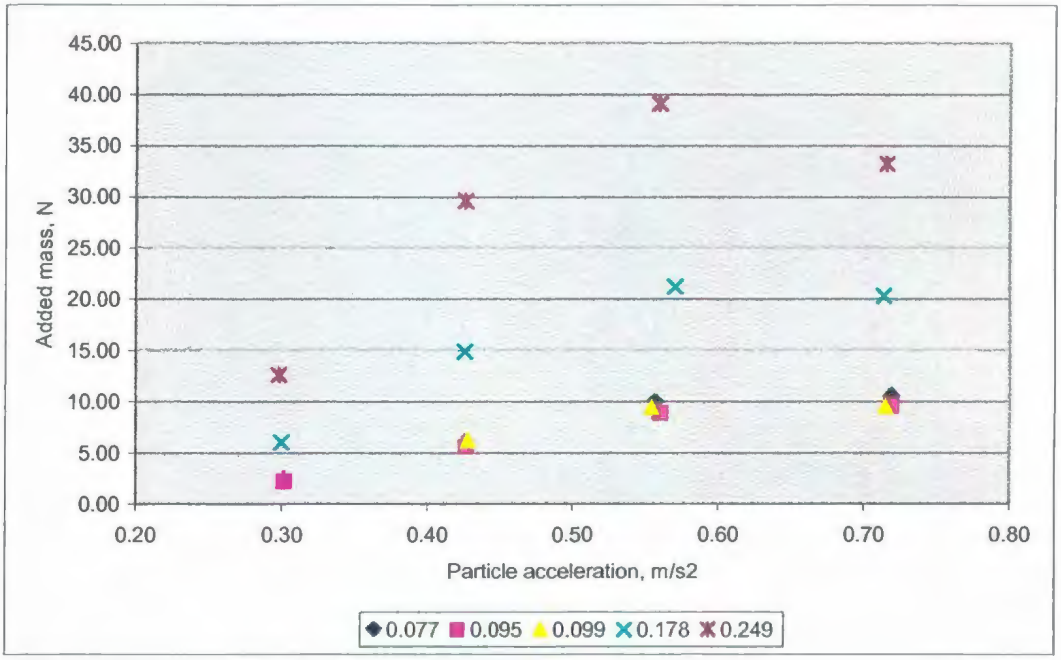

Fig. 3.15 The added mass component of the total wave force vs. particle velocity

Total wave force and the resulting drag and added mass components are plotted in Fig. 3.13-15. It can be seen that overall hydrodynamic loads increase sensibly as the nets get less porous and particle velocity or acceleration increases; however, drag force appears more scattered.

3.2.2 Drag coefficient in oscillating flow

As mentioned previously, the drag coefficient for a cylinder in oscillating flow is conventionally considered as a function of the Keulegan-Carpenter (KC) and Reynolds numbers [7]. This dependence is also shown in Fig. 3.16.

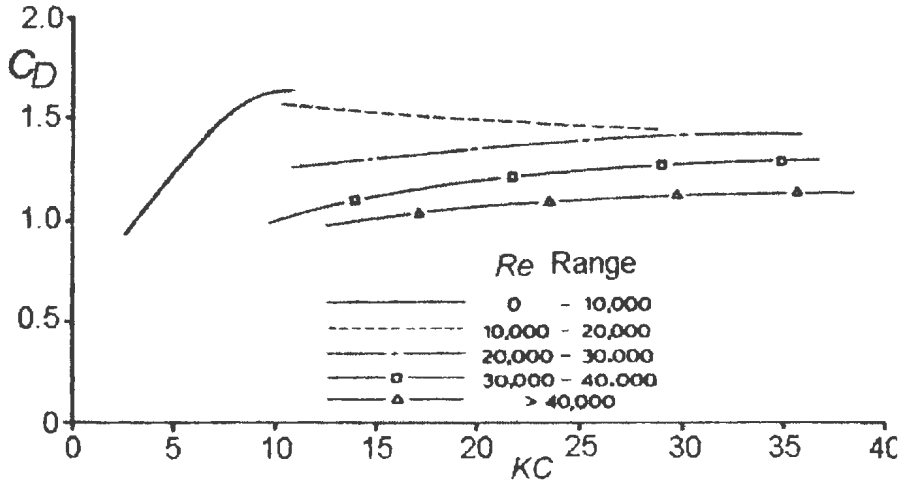

Fig. 3.16 Drag coefficients for an oscillating vertical cylinder from [7]

It can be seen from Fig. 3.16 that for Reynolds numbers below 10,000, the drag coefficient strongly depends on the Keulegan-Carpenter number in comparison to Reynolds numbers over 10,000 for which drag coefficient only changes slightly even with significant change in the Keulegan-Carpenter number.

Due to the relatively small twine diameter of the nets, as illustrated in Fig. 3.17, the Keulegan-Carpenter number appears on a much larger scale in comparison to cylinders tested by Chakrabati [7]. It can also be observed that the drag coefficient for nets changes significantly even with a slight change in the

Keulegan-Carpenter number; and for larger twine diameters, the curves appear to be close to vertical lines, which might indicate an independence of the drag coefficient from the Keulegan-Carpenter number.

The curves also appear to be unaffected by net porosity. However, this does not make physical sense as drag increases as the net gets denser.

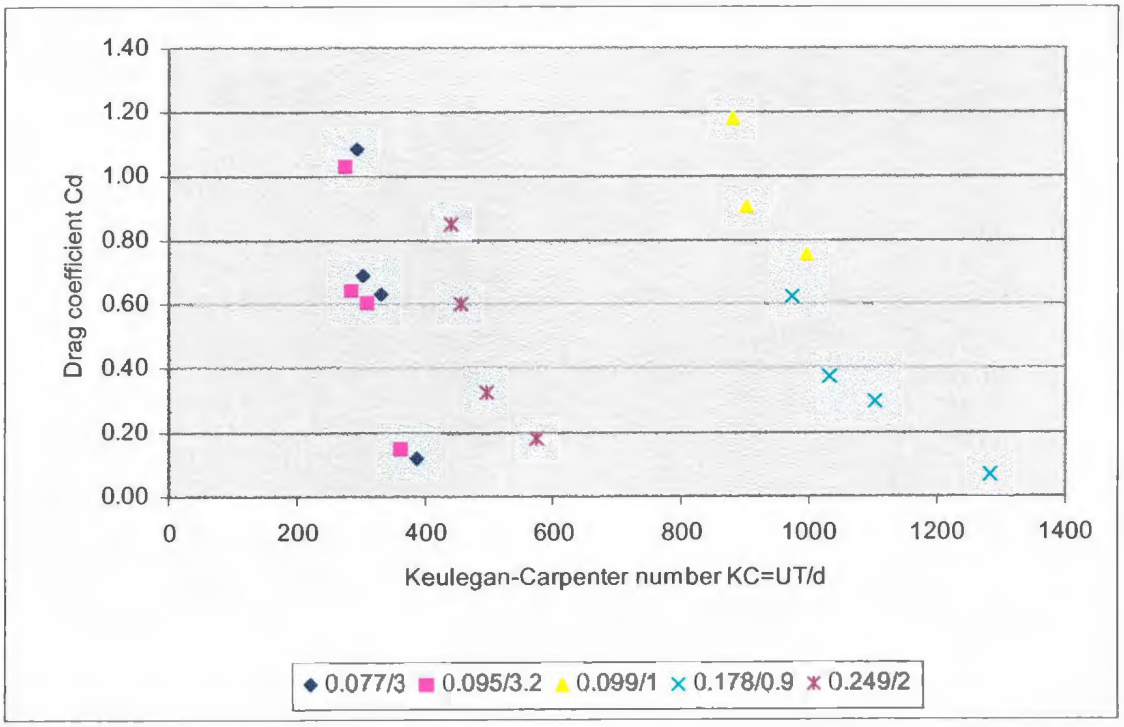

Fig. 3.17 Drag coefficient in oscillating flow vs. the Keulegan-Carpenter number (the legend specifies net solidity as a first number and twine diameter in mm as a second number for each sample)

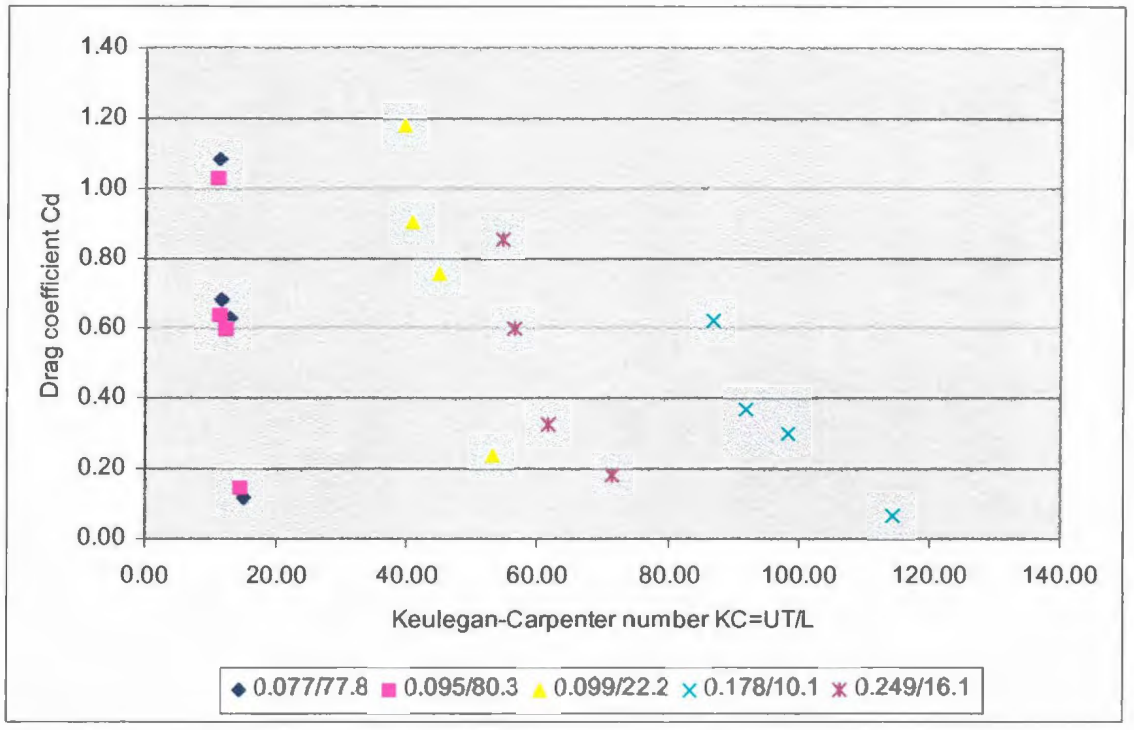

Fig. 3.18 Drag coefficient in oscillating flow vs. the Keulegan-Carpenter number (the legend specifies net solidity as a first number and mesh size in mm as a second number for each sample)

Considering mesh size as a characteristic dimension for the Keulegan-Carpenter number (Fig 3.18) demonstrates the dependence of drag coefficient on mesh size. Thus, since twine diameter and mesh size form net solidity and each of them individually impacts drag coefficient, net solidity should influence drag coefficient as well. The independence of drag coefficient from net porosity shown on Fig 3.19 might be caused by effectively accounting for twine diameter twice: in the Keulegan-Carpenter number and net solidity.

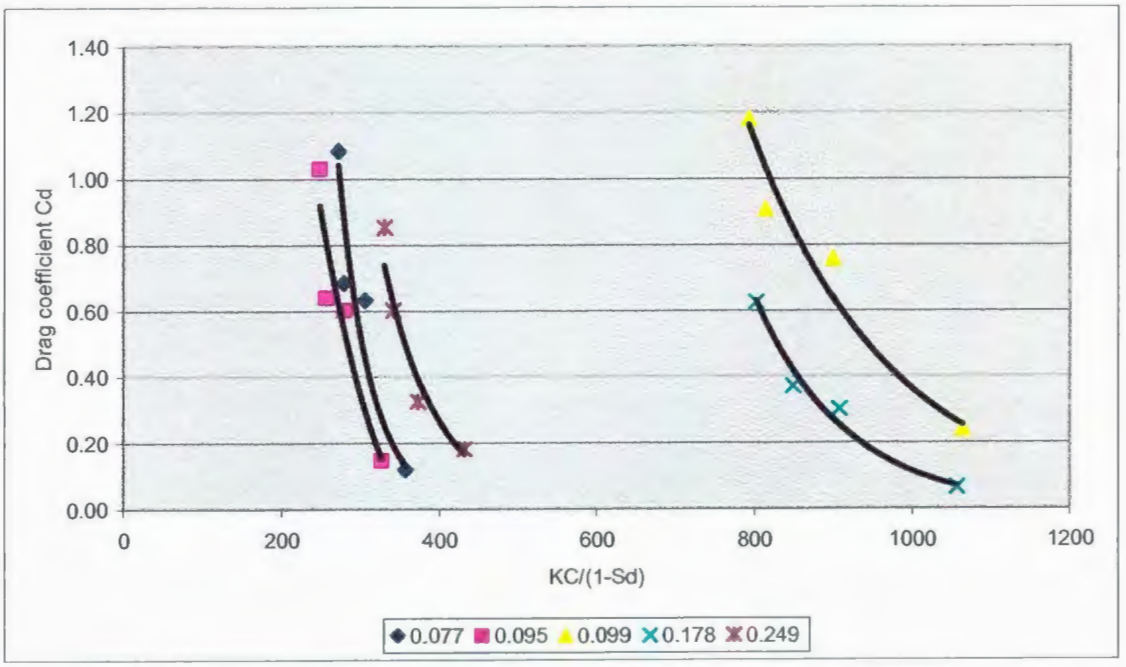

Fig. 3.19 Drag coefficient in oscillating flow vs. the ratio of the Keulegan-Carpenter number and net porosity (the legend presents net solidity)

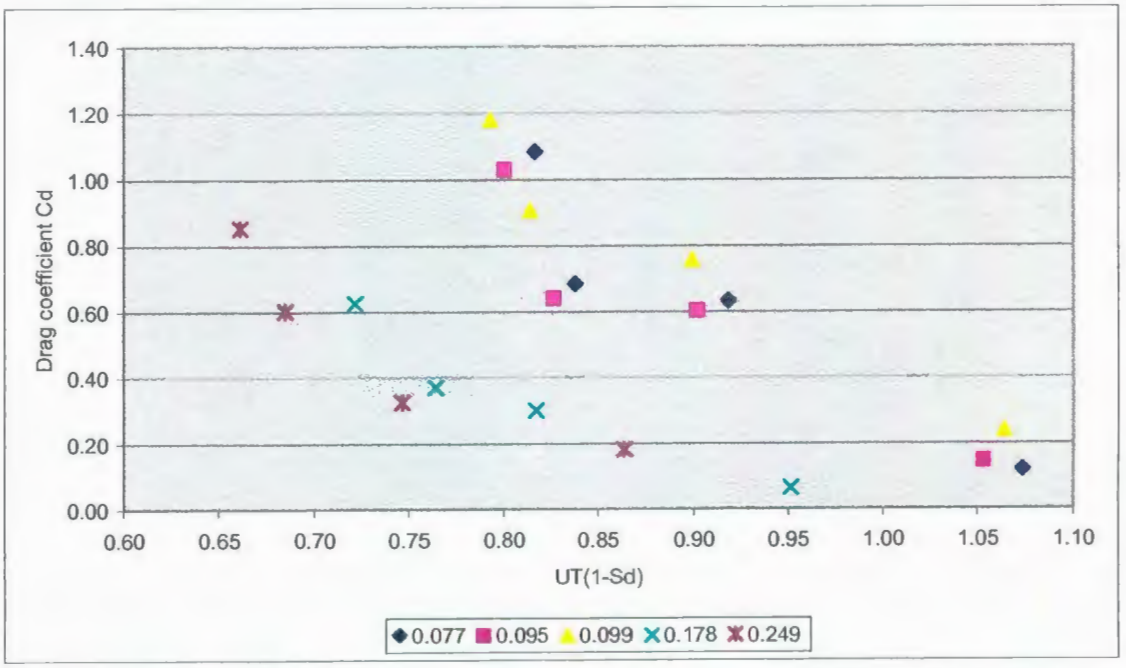

Fig. 3.20 Drag coefficient in oscillating flow as a function of particle velocity, wave period and net porosity

Fig. 3.20 also gives weight to this supposition. Although the data is a bit scattered, it illustrates trends for two groups of nets: with low and high solidity.

Thus, it appears that drag coefficient might not be able to be expressed through a non-dimensional parameter, as both geometrical parameters have to be taken into account. As a suggestion, the drag coefficient in oscillating flows may be estimated as the ratio of particle velocity, wave period and a square root of net porosity (Fig 3.21). As can be seen, this function collapses two groups of solidities together with a reasonable error; however, further experimental work should be conducted for validation.

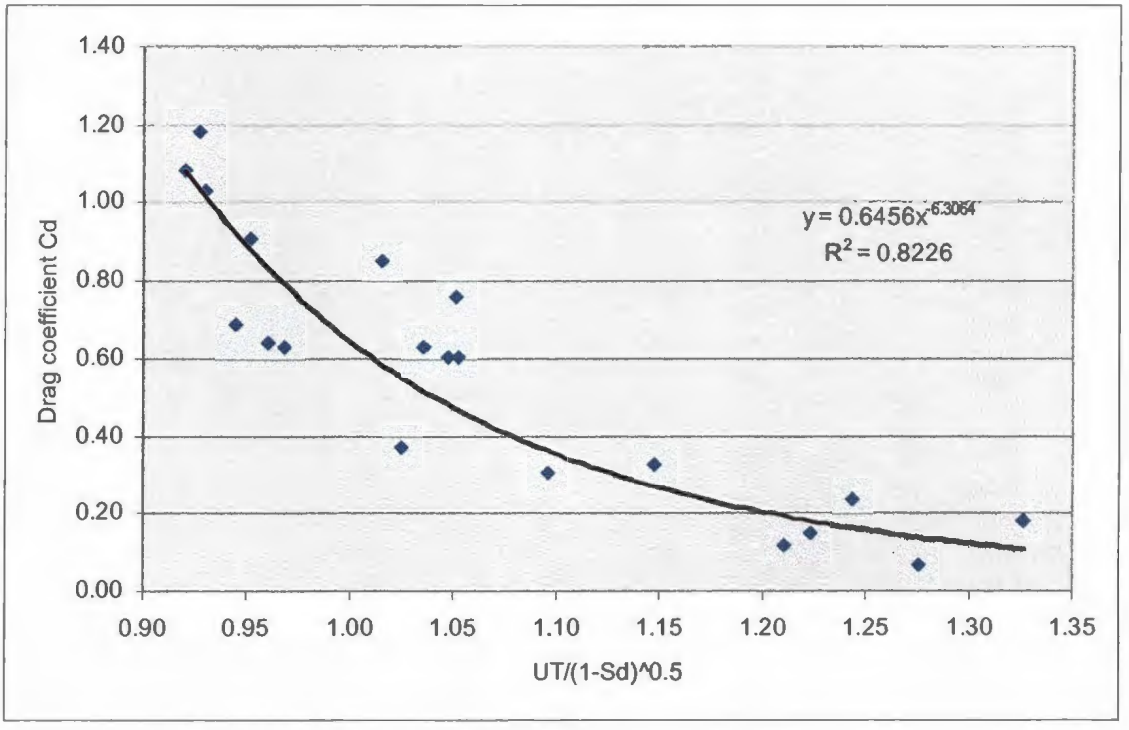

Fig. 3.21 Drag coefficient in oscillating flow as a function of particle velocity, wave period and modified net porosity

3.2.3 Added mass estimation

The inertia or added mass coefficient is estimated as a function of the Keulegan-Carpenter number. Since twine diameter is very small, added mass coefficients for nets appear to be on an unusually large scale: in the hundred thousands (Fig. 3.22). It can also be seen that added mass coefficient as a function of the Keulegan-Carpenter number is independent from twine diameter or net solidity.

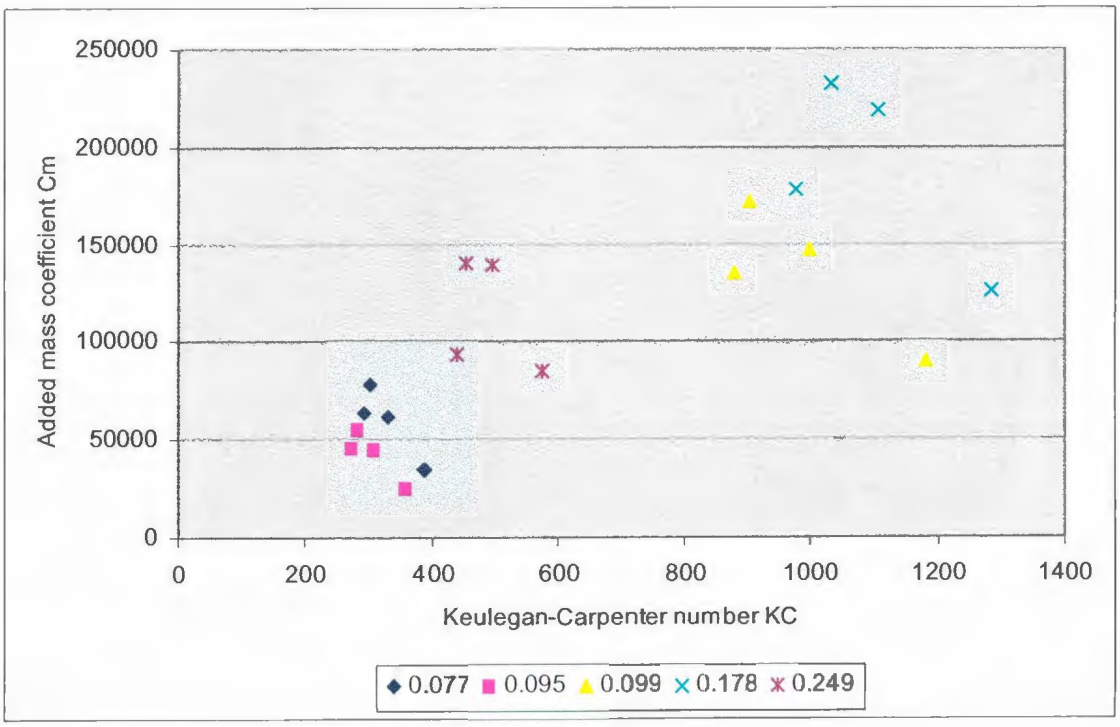

Fig. 3.22 Added mass (inertia) coefficient as a function of the Keulegan-Carpenter number

In the previous sub-chapter it was shown that the conventional approach to estimate added mass through the Keulegan-Carpenter number might be not

applicable to nets because more than one geometrical parameter characterizes hydrodynamic loads. It is also uncertain how to assess the amount of water affected by the net due to compliance. Presumably the affected area equals the total net projected area. Then from Newton's law of motion, the affected thickness (equivalent mass) of water can be estimated as:

$$\delta = \frac{F_A}{A_p \rho \dot{U}} \tag{3.17}$$

where F_A is added mass, A_p is projected area, $\dot{U}$ is particle acceleration.

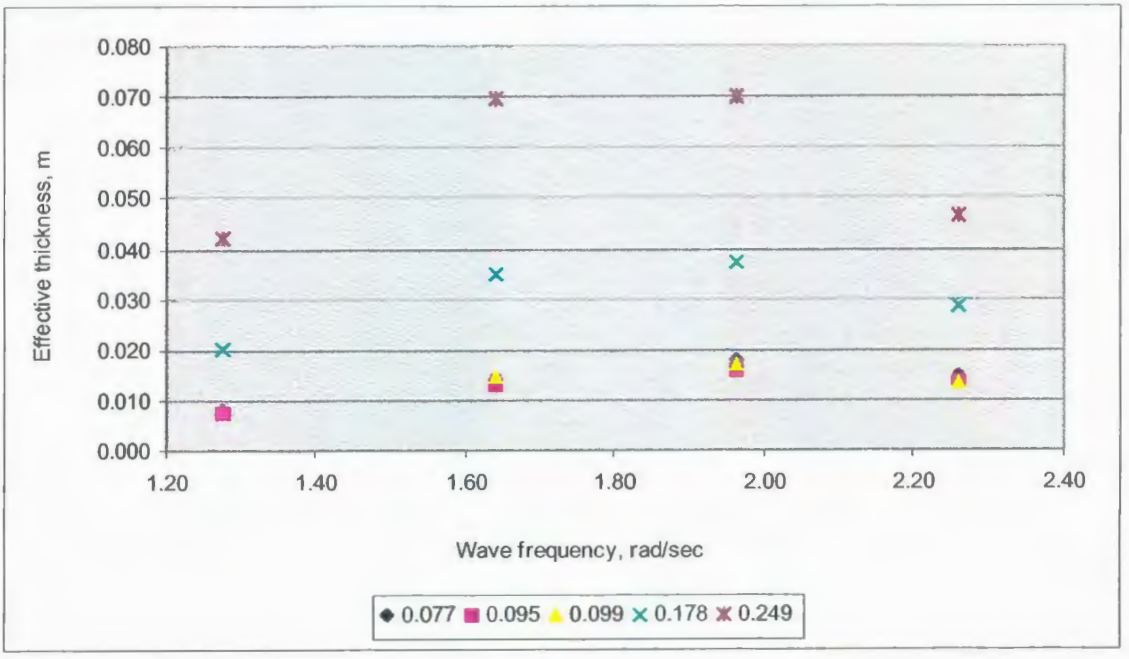

Fig. 3.23 Effective thickness vs. wave frequency

Since the experiment was conducted with full-scale nets, it is assumed that a dimensional parameter, such as the effective thickness, can be used to express added mass for nets. Wave frequency is a major determinant for particle acceleration, so it seems sensible to consider the dependence of effective thickness on frequency (Fig. 3.23). It can be seen that the effective thickness increases as wave frequency increases (waves become shorter, and in this experiment also less steep). However, after approximately 2rad/sec, the effective thickness decreases, especially for less porous nets, which is a common trend for bodies in oscillating flows. It also appears that effective thickness depends on net solidity.

Thus, it is suggested that added mass for nets can be estimated as a function of wave frequency and net solidity. Expressing the added mass in terms of effective thickness over the net area also offers a more intuitive measure of the added mass effect than coefficients based on the displacement of the net twine.

IV. Conclusions and further work

Two experiments were conducted to estimate the hydrodynamic loads on five plane net samples in steady and oscillating flows. A new empirical formula is suggested as a function of net porosity and drag coefficient for a cylinder (and a sphere for knotted nets). The advantage of the formula in comparison to the existing ones is that it incorporates the well-established drag coefficient of a cylinder and thus it is less limited in Reynolds number. The inclusion of the drag coefficient for a cylinder should naturally allow the application of the formula for different angles of attack as well; however, it is recommended to verify this presumption with another experiment, where net samples are tested over a range of angles of attack.

The interaction effect of net solidity and water velocity was disclosed by applying a two-factorial experimental design. This analysis is meant to disclose effects by assuming their nature is linear only. However, the Response Surface Method (Montgomery 1995) can be applied in the future to establish a polynomial formula for predicting steady flow drag as a function of net solidity and current velocity.

It was also found that conventional non-dimensional parameters for drag and inertia coefficients in oscillating flow are probably not applicable for nets. It is suggested that drag coefficient is perceived as a function of wave particle velocity and net porosity. For further verification it is recommended to

experimentally study the individual influence of wave particle velocity and wave period on drag. Wave period is a function of wavelength, but particle velocity is a function of wave period and amplitude. Thus, the same wavelength can be maintained for different velocities if the wave amplitude changes.

A new parameter was introduced for added mass estimation: effective thickness, a width of water notionally affected by the net as a function of particle velocity and net porosity. This parameter offers an intuitive improvement over conventional concepts of added mass coefficients related to the mass or displacement of the physical body, in this case the net twine, but the data set collected as part of this study does not provide a definitive proof of the utility of the concept. Thus, it is recommended to conduct another experiment for a wider range of wave frequencies to establish a formula for added mass estimation through effective thickness which is a function of net porosity and wave frequency.

References

[1] Aarnes J.V., Rudi H. and Loland G. (1990) "Current Forces on Cage, Net Deflection", *"Engineering for Offshore Fish Farming", Proceedings of the conference organized by the Institution of Civil Engineers, and held in Glasgow on 17-18 October 1990,* Thomas Telford, London

[2] Armour J.C. and Cannon J.N. (1968) "Fluid Flow Through Woven Screens", *AIChE Journal,* Vol. 14, No. 3

[3] Blevins R.D. (1984) "Applied Fluid Dynamics Handbook", Krieger Publishing Company, Florida

[4] Bris F.L., Marichal D. (1998) "Numerical and Experimental Study of Submerged Supple Nets: Applications to Fish Farms", *Journal of Marine Science and Technology*

[5] Berteaux H.O. (1976) Bouy Engineering. John Wiley and Sons, USA

[6] Carrothers P.J.G. and Baines W.D. (1965) "Forces on Screens Inclined to a Fluid Flow", *Transactions of the ASME*

[7] Chakrabarti S.K. (2002) "The Theory and Practice of Hydrodynamics and Vibration", Offshore Structure Analysis, Inc, USA

[8] Fredriksson D.W., Palczynski M.J., Irish J.D., Swift M.R. and Celikkol B. (2003) "Fluid Dynamic Drag Modeling of a Central Spar Cage", "Open Ocean Aquaculture. From research to Commercial Reality", The World Aquaculture Society

[9] Freedman A.L. (1973) Theory and Design of Commercial Fishing Gears. IPST, Jerusalem

[10] Koo J.-K., James D.F. (1973) "Fluid Flow Around and Through a Screen", *Journal of Fluid Mechanics Digital Archive,* Cambridge University Press

[11] Lader P.F. and Enerhaug B. (2005) "Experimental Investigation of Forces and Net Geometry of a Net Cage in Uniform Flow", *IEEE Journal of Ocean Engineering*, Vol. 30, No. 1

[12] Loland G. (1993) "Current Forces on, and Water Flow Through and Around, Floating Fish Farms", Aquaculture International 1

[13] Manuza M. (1995) "Hydrodynamic Forces of Floating Offshore Aquaculture Cages", Master thesis, University of Maine

[14] Milne P. H. (1979) "Fish and Shellfish Farming in Coastal Waters", Fishing News Books Ltd, England

[15] Montgomery D.C. and Myers R.H(1995) "Response Surface Methodology", John Wiley and Sons Inc.

[16] Sharp J.J. (1981) "Hydraulic Modeling", Butterworths

[17] White F. (1974) "Viscous Fluid Flow", McGraw Hill

Appendix I Steady flow experiment data

No Net Installed

Towing speed	Dir	T1	T2	L1	L2	Force
0,1	F	-16,478	-16,24	-16,477	-16,255	-0,014
0,2	F	-16,504	-16,286	-16,511	-16,287	-0,008
0,5	F	-16,551	-16,287	-16,542	-16,206	0,09
1	F	-16,588	-16,297	-16,677	-16,474	-0,266
2	F	-16,586	-16,297	-17,249	-17,059	-1,425
0,1	R	-16,556	-16,281	-16,551	-16,266	0,02
0,2	R	-16,563	-16,281	-16,576	-16,297	-0,029
0,5	R	-16,565	-16,273	-16,527	-16,399	-0,088
1	R	-16,595	-16,315	-16,823	-16,304	-0,217

Sample 1, Sd=0,077

Towing speed	Dir	T1	T2	L1	L2	Tare	Force
0		-16,57	-16,112	-16,57	-16,113	0,000	0,001
0,5	F	-16,665	-16,188	-8,9796	-8,6922	-0,095	15,277
0,1	F	-16,643	-16,141	-16,302	-15,817	-0,006	0,671
0,1	R	-16,642	-16,123	-16,945	-16,424	-0,006	0,598
0,2	F	-16,632	-16,131	-15,473	-14,989	-0,018	2,319
0,2	R	-16,664	-16,139	-17,775	-17,263	-0,018	2,217
0,5	F	-16,667	-16,143	-8,9076	-8,5689	-0,095	15,429
0,5	R	-16,655	-16,138	-24,061	-23,519	-0,095	14,692
0,749	F	-16,679	-16,151	-1,3335	-1,2298	-0,204	30,471
0,745	R	-16,6	-16,091	-32,422	-31,423	-0,202	30,952
0,998	F	-16,629	-16,099	10,68	10,472	-0,354	54,234
0,993	R	-16,568	-16,075	-44,108	-40,474	-0,351	51,588
1,485	F	-16,604	-16,076	40,967	39,852	-0,766	114,265
1,899	F	-16,599	16,086	75,227	72,218	-1,238	149,196

Sample 2, Sd=0,095

0,1	F	-17,17	-16,893	-16,887	-16,714	-0,006	0,468
0,1	R	-17,188	-17,196	-17,526	-17,523	-0,006	0,659
0,2	F	-17,127	-17,094	-15,879	-15,865	-0,018	2,495
0,2	R	-17	-16,97	-18,319	-18,269	-0,018	2,600
0,5	F	-17,186	-17,169	-9,0123	-8,7446	-0,095	16,694
0,5	R	-16,979	-16,931	-25,335	-25,144	-0,095	16,474
0,749	F	-17,042	-16,985	-1,422	-1,1816	-0,204	31,628
0,746	R	-16,944	-16,862	-35,408	-35,085	-0,203	36,484
0,998	F	-17,002	-16,911	11,257	12,158	-0,354	57,682
0,994	R	-16,819	-16,765	-51,246	-50,186	-0,352	67,496
1,494	F	-16,929	-16,828	47,167	49,523	-0,775	131,222
1,992	F	-16,82	-16,731	88,001	101,8	-1,360	224,712

Sample 3, Sd=0,099

Towing speed	Dir	T1	T2	L1	L2	Tare	Force
0,1	F	-16,424	-16,183	-16,042	-15,871	-0,006	0,700
0,1	R	-16,502	-16,401	-16,95	-16,836	-0,006	0,877
0,2	F	-16,433	-16,33	-14,858	-14,76	-0,018	3,163
0,2	R	-16,564	-16,394	-18,222	-18,07	-0,018	3,316
0,5	F	-16,522	-16,378	-7,2879	-6,8689	-0,095	18,839
0,5	R	-16,578	-16,39	-26,369	-26,34	-0,095	19,646
0,749	F	-16,572	-16,385	2,1256	2,7215	-0,204	38,009
0,746	R	-16,597	-16,399	-37,015	-36,774	-0,203	40,590
0,998	F	-16,567	-16,36	16,564	16,629	-0,354	66,474
0,994	R	-16,578	-16,396	-53,526	-53,269	-0,352	73,469
1,494	F	-16,579	-16,369	60,542	59,932	-0,775	154,197
1,992	F	-16,584	-16,376	95,563	116,39	-1,360	246,273

Sample 4, Sd=0,178

0,1	F	-16,553	-15,536	-15,749	-14,953	-0,006	1,393
0,1	R	-16,604	-16,38	-17,548	-17,357	-0,006	1,915
0,2	F	-16,356	-15,907	-13,447	-13,145	-0,018	5,689
0,2	R	-16,573	-16,496	-20,051	-19,864	-0,018	6,828
0,5	F	-16,466	-16,387	1,296	1,2151	-0,095	35,460
0,5	R	-16,607	-16,501	-36,677	-35,574	-0,095	39,048
0,749	F	-16,473	-16,377	18,713	18,358	-0,204	70,125
0,998	F	-16,439	-16,313	44,689	44,272	-0,354	122,067
0,994	R	-16,643	-16,473	-89,9	-85,862	-0,352	142,294
1,494	F	-16,418	-16,289	100,83	117,13	-0,775	251,442
1,992	F	-16,55	-16,356	180,81	225,75	-1,360	440,826

Sample 5, Sd=0,249

0,1	F	-16,255	-15,766	-15,145	-14,726	-0,006	2,156
0,1	R	-16,476	-16,187	-18,2	-17,836	-0,006	3,367
0,2	F	-16,305	-15,97	-11,898	-11,69	-0,018	8,705
0,2	R	-16,626	-16,244	-22,449	-21,916	-0,018	11,477
0,5	F	-16,412	-16,036	10,59	10,106	-0,095	53,239
0,5	R	-16,613	-16,142	-45,449	-44,888	-0,095	57,487
0,749	F	-16,578	-16,095	38,164	36,394	-0,204	107,435
0,745	R	-16,621	-16,129	-75,954	-75,455	-0,202	118,457
0,997	F	-16,565	-16,081	79,366	75,452	-0,354	187,818
0,994	R	-16,569	-16,131	-120,28	-118,74	-0,352	205,968
1,494	F	-16,575	-16,077	195,48	188,54	-0,775	417,447
1,992	F	-16,591	-16,126	351,91	391,5	-1,360	777,487

Appendix II Oscillating flow experiment data

	wave length	wave amplitude	wave steepness	wave number	analytical wave frequency	experimental wave frequency	experimental horisontal particle velocity at depth of 1m	velocity phase shift
	λ	A	λ/A	k	ωan	ωex	Uexp	φ_u
	m	m	-	-	rad/sec	rad/sec	m/s	-
sample1 Sd=0.077	10,2	0,18	0,018	0,62	2,26	2,26	0,29	0,08
	12,35	0,15	0,012	0,51	1,96	1,96	0,29	6,08
	15,4	0,13	0,009	0,41	1,64	1,64	0,26	5,07
	20,5	0,11	0,006	0,31	1,28	1,28	0,14	0,51
sample2 Sd=0.095	10,2	0,18	0,018	0,62	2,26	2,26	0,29	6,21
	12,35	0,15	0,012	0,51	1,96	1,96	0,29	5,19
	15,4	0,13	0,009	0,41	1,64	1,64	0,27	4,99
	20,5	0,11	0,006	0,31	1,28	1,28	0,16	5,88
sample3 Sd=0.099	10,2	0,18	0,018	0,62	2,26	2,26	0,29	6,11
	12,35	0,15	0,012	0,51	1,96	1,96	0,29	0,36
	15,4	0,13	0,009	0,41	1,64	1,64	0,27	5,73
	20,5	0,12	0,01	0,310	1,28	1,28	0,16	0,33
sample4 Sd=0.178	10,2	0,18	0,018	0,62	2,26	2,26	0,29	1,10
	12,35	0,16	0,013	0,51	1,96	1,96	0,28	6,02
	15,4	0,13	0,009	0,41	1,64	1,64	0,24	6,10
	20,5	0,11	0,006	0,31	1,28	1,28	0,12	0,64
sample5 Sd=0.249	10,2	0,18	0,018	0,62	2,26	2,26	0,29	0,76
	12,35	0,15	0,012	0,51	1,96	1,96	0,28	5,60
	15,4	0,13	0,009	0,41	1,64	1,64	0,26	5,81
	20,5	0,11	0,006	0,31	1,28	1,28	0,15	0,29

	analytical horizontal particle velocity at depth of 1 m	analytical horizontal particle velocity, integrated average	experimental horizontal particle acceleration, differential of velocity	acceleration phase shift	analytical acceleration, integrated average	total force	force phase shift	drag force
	Uan	Uan av	Úexp	φ_u	Úan	Ft	φ_f	Fd
	m/s	m/s	m/s2	-	m/s2	N	-	N
sample1 Sd=0.077	0,31	0,32	0,66	1,65	0,72	11,39	5,98	4,22
	0,28	0,28	0,56	1,37	0,56	10,22	5,87	2,12
	0,26	0,26	0,42	0,36	0,43	6,28	4,81	1,64
	0,24	0,24	0,18	2,09	0,30	2,45	0,41	0,26
sample2 Sd=0.095	0,31	0,32	0,66	1,50	0,72	10,82	5,74	4,96
	0,28	0,29	0,58	0,47	0,56	9,27	4,92	2,48
	0,26	0,26	0,45	0,28	0,43	5,96	4,66	1,94
	0,24	0,24	0,20	1,17	0,30	2,26	5,71	0,39
sample3 Sd=0.099	0,31	0,32	0,66	1,40	0,72	11,22	5,56	5,86
	0,28	0,28	0,57	1,93	0,55	10,12	0,00	3,58
	0,26	0,26	0,45	1,06	0,43	6,75	5,35	2,55
	0,24	0,24	0,20	1,91	0,30	2,77	0,09	0,68
sample4 Sd=0.178	0,31	0,32	0,67	2,67	0,71	21,09	0,83	5,57
	0,29	0,29	0,55	1,31	0,57	21,44	5,89	2,80
	0,26	0,26	0,40	1,39	0,43	15,05	5,98	1,82
	0,23	0,24	0,16	2,21	0,30	6,08	0,69	0,33
sample5 Sd=0.249	0,31	0,32	0,66	2,33	0,72	34,88	0,45	10,65
	0,28	0,28	0,55	0,90	0,56	39,59	5,45	6,09
	0,26	0,26	0,44	4,82	0,43	29,72	5,71	2,73
	0,23	0,23	0,20	1,86	0,30	12,68	0,39	1,24